

# On the formation of H $\alpha$ line emission around classical T Tauri stars

Ryuichi Kurosawa<sup>1\*</sup>, Tim J. Harries<sup>1</sup> and Neil H. Symington<sup>2</sup>

<sup>1</sup>School of Physics, University of Exeter, Stocker Road, Exeter EX4 4QL.

<sup>2</sup>School of Physics and Astronomy, University of St. Andrews, North Haugh, St. Andrews, Fife, KY16 9SS.

Dates to be inserted

## ABSTRACT

We present radiative transfer models of classical T Tauri stars, and investigate the formation of H $\alpha$  line emission in order to understand their complex circumstellar environments, and to explain the wide variety of line profiles seen in observations. To overcome the limited applicability of the radiative transfer models with magnetospherical accretion alone to fitting observed H $\alpha$  profiles, and to any other lines affected by the stellar wind, two types of kinematic wind models are introduced: (1) the bipolar wind model in which the wind is originated from the star itself, and (2) the disc-wind model in which the wind originates from the inner part of the accretion disc. We perform systematic investigations of the model parameters for the wind and the magnetosphere to search for possible geometrical and physical conditions which lead to the types of profiles seen in observations. We find both wind models can reproduce the wide range profile types seen in observations, although the inclination dependence of the line equivalent width predicted by the bipolar wind model agree with trends seen in the observation, but the disc-wind model does not. Using the model results, we examine the H $\alpha$  spectroscopic classification used by Reipurth et. al., and discuss the basic physical conditions required to reproduce the profiles in each classified type.

**Key words:** stars: formation – circumstellar matter – radiative transfer – stars: pre-main-sequence

## 1 INTRODUCTION

T Tauri stars (TTS) are young ( $<\sim 3 \times 10^6$  yrs, Appenzeller & Mundt 1989) low-mass objects, and are the progenitors of solar-type stars. Classical T Tauri stars (CTTS) exhibit strong H $\alpha$  emission, and typically have spectral types of F–K. Some of the most active CTTS show emission in higher Balmer lines and metal lines (e.g., Ca II H and K). They also exhibit excess continuum flux in the ultraviolet (UV) and infrared (IR). Their spectral energy distribution and polarisation data suggest the presence of circumstellar discs, which plays an important role in regulating dynamics of gas flows around CTTS (e.g. Camenzind 1990).

Many observational studies (e.g., Herbig 1962; Edwards et al. 1994; Kenyon et al. 1994; Reipurth, Pedrosa, & Lago 1996; Alencar & Basri 2000) of CTTS line profiles show evidence for both outward wind flows and inward accretion flows, as seen in the blue-shifted absorption features in H $\alpha$  profiles and the redshifted inverse P Cygni (IPC) profiles respectively. Typical mass-loss rates of CTTS are about  $10^{-9} M_{\odot} \text{ yr}^{-1}$  to  $10^{-7} M_{\odot} \text{ yr}^{-1}$  (e.g., Kuhí 1964; Edwards et al. 1987; Hartigan, Edwards, & Ghandour 1995), and the mass-accretion rates are also about  $10^{-9} M_{\odot} \text{ yr}^{-1}$  to  $10^{-7} M_{\odot} \text{ yr}^{-1}$  (e.g., Kenyon & Hartmann 1987; Bertout, Basri, & Bouvier 1988; Gullbring et al. 1998). Recent H $\alpha$  spectro-

astrometric observations by Takami, Bailey, & Chrysostomou (2003) show direct evidence for the presence of bipolar and monopolar outflows down to  $\sim 1$  au scale (e.g. CS Cha and RU Lup). Similarly, ESO VLT observations using high-resolution ( $R = 50\,000$ ) two-dimensional spectra of edge-on CTTS (HH30\*, HK Tau B, and HV Tau C) by Appenzeller et al. (2005) show the extended H $\alpha$  emission in the direction perpendicular to the obscuring circumstellar disc both above and below the disc, suggesting the presence of the bipolar outflows. On a larger scale, *HST* observations of HH30 (Burrows et al. 1996) show the jet traced to within  $\lesssim 30$  au from the star. The jet has a cone shape with an opening angle of  $3^\circ$  between 70 and 700 au (Königl & Pudritz 2000). Alencar & Basri (2000) found about 80 per cent of their sample (30 CTTS) show blue-shifted absorption components in at least one of the Balmer lines and Ca K (most commonly in H $\alpha$ ).

In the currently favoured model of accretion in CTTS, the accretion disc is disrupted by the magnetosphere of stars which channels the gas from the disc onto the stellar surface (e.g., Uchida & Shibata 1985; Königl 1991; Collier Cameron & Campbell 1993; Shu et al. 1994). This picture is supported by the evidence that CTTS have relatively strong ( $\sim 10^3$  G) magnetic field (e.g., Johns-Krull et al. 1999; Guenther & Emerson 1996; Symington et al. 2005b) and by radiative transfer models which reproduce the observed profiles for some TTS (Muellerolle, Calvet, & Hartmann 2001). The magnetospherical accretion model naturally explains

\* E-mail:rk@astro.ex.ac.uk

the blue-ward asymmetric emission lines (seen in some of CTTS) caused by the partial occultation of the flow by the stellar disc, and the redshifted absorption component at the typical free-fall velocities (a few hundred km s<sup>-1</sup>) seen in some of CTTS. Despite the success of the magnetospherical accretion model in explaining the line profiles in some CTTS, the overwhelming observational evidence for outflow (mentioned above) in the CTTS profiles suggests that this model is only a part of the complete picture. Clearly, a modification to include an out-flowing wind/jet flow is necessary if one wishes to predict the mass-accretion rate and the mass-loss rate of CTTS by modelling their emission profiles (e.g. H $\alpha$ ).

Prior to the magnetospherical paradigm, many alternative models had been considered to explain the observed spectroscopic features mentioned earlier. For example, (1) the Alfvén wave-driven wind model (e.g. Decampli 1981; Hartmann, Avrett, & Edwards 1982), (2) turbulent boundary layer (between the accretion disc and stellar surface) model (e.g. Bertout et al. 1988; Basri & Bertout 1989), (3) chromospheric model (e.g. Calvet, Basri, & Kuhí 1984), and (4) disc wind model (e.g. Calvet, Hartmann, & Hewett 1992; Kwan & Tademaru 1995). Recent work by Alencar et al. (2005) showed the observed H $\alpha$ , H $\beta$  and Na D lines of RW Aur are better be produced by the radiative transfer model which includes a collimated disc-wind arising from near the inner edge of the accretion disc. Malbet et al. (2005) considered a combination of a spherical wind and an accretion disc in their radiative transfer model to reproduce Br $\gamma$  from the early-type Herbig Be star MWC 297.

The magneto-centrifugal wind model, first proposed by Blandford & Payne (1982), has been often used to reproduce the large-scale wind structure of T Tauri stars, or to model observed optical jets (e.g. HH 30 jet by Burrows et al. 1996; Ray et al. 1996). The launching of the wind from a Keplerian disc is typically done by treating the equatorial plane of the disc as a mass-injecting boundary condition (e.g., Shu et al. 1994; Ustyugova et al. 1995; Ouyed & Pudritz 1997; Krasnopol'sky et al. 2003). Depending on the location of the open magnetic fields anchored to the disc, two different types of winds are produced. If the field is constrained to be near the co-rotation radius of stellar magnetosphere, an “X-wind” (Shu et al. 1994) is produced. If the open field lines are located in a wider area of the disc, a “disc-wind” similar to Königl & Pudritz (2000) is produced Krasnopol'sky et al. (2003). Recent reviews on the jet/wind-disc connection can be found in Königl & Pudritz (2000) and Pudritz & Banerjee (2005). Interestingly, Matt & Pudritz (2005) showed the possibility that the stellar wind along the open magnetic field originated from the star can cause significant spin-down torque on the star, provided that mass-loss rate is high enough.

The main aim of this paper is to find a simple kinematic model which can reproduce the wide variety of the observed profiles, and to perform the empirical studies of the line formation. More specifically, we present disc–wind–magnetosphere hybrid models for CTTS, and perform parametric studies of the H $\alpha$  formation. This study should provide preliminary physical conditions which lead to the wide variety of emission line profiles seen in the observation, and will help to construct more comprehensive circumstellar models (e.g. via MHD simulations) of T Tauri stars. Using the model results, we examine the H $\alpha$  spectroscopic classification used by Reipurth et al. (1996), and compare models with observations. We will also discuss whether our model is consistent with some predictions made by the recent MHD studies i.e.  $\mu = \dot{M}_{\text{wind}}/\dot{M}_{\text{acc}} \approx 0.1$  (e.g. Königl & Pudritz 2000).

In section 2, the model assumptions, and the basic model configurations are presented. We discuss the radiative transfer model

used to compute the profiles in section 3, and the results of model calculations are given in section 4. The closer examination and discussion of the results are presented in section 5. Finally, the summary of this work and the conclusion are in section 6.

## 2 MODEL CONFIGURATION

To understand how the different part of the CTTS circumstellar environment contributes to the formation of H $\alpha$ , the model space is divided into four different regions: (1) a central continuum source, (2) the magnetospherical accretion flow, (3) the wind outflow, and (4) the accretion disc. Fig. 1 depicts the relative location of the regions in the model space. In all regions, the density is symmetric around the z-axis. The innermost radius of the magnetosphere at the equatorial plane coincides with the inner radius of the accretion disc. From the innermost part of the accretion disc, the gas falls freely, moving along the magnetic field onto the surface of the star. For simplicity, the out-flowing wind component is defined only in the outside of the largest radius of the magnetosphere (to avoid overlapping of the wind with the magnetosphere). In the following subsections, the details of model components will be described.

### 2.1 Continuum Source

Unless specified otherwise, we adopt stellar parameters of a typical classical T Tauri star for the central continuum source, i.e. radius ( $R_*$ ), mass ( $M_*$ ), and effective temperature the photosphere ( $T_{\text{ph}}$ ) are  $2 R_\odot$ ,  $0.5 M_\odot$ , and 4000 K respectively. The model atmosphere of Kurucz (1993) with  $T_{\text{ph}} = 4000$  K and  $\log g_* = 3.5$  (cgs) is used to find the photospheric continuum at the H $\alpha$  wavelength. The parameters are summarised in Table 1.

For a model which includes magnetospherical accretion, an additional continuum source is considered. As the in-falling gas becomes close to the stellar surface, it is decelerates in a strong shock, and is heated to  $\sim 10^6$  K. The X-ray radiation produced in the shock will be absorbed by the gas locally, and re-emitted in optical and UV radiation (Königl 1991; Hartmann, Hewett, & Calvet 1994). This will create hot rings near the stellar surface where the magnetic field intersects with the surface. For simplicity, the free-falling kinetic energy is assumed to be thermalized in the radiating layer, and re-emits as blackbody radiation (with a single temperature). With the parameters of the magnetosphere and the star given above (Table 1), about 8 per cent of the surface is covered by the hot rings. If the mass-accretion rate is  $10^{-7} M_\odot \text{ yr}^{-1}$ , the ratio of this accretion luminosity to the photospheric luminosity is about 0.5, and the corresponding temperature of the hot rings is about 6400 K. The continuum emission from the hot rings is taken into account when computing the line profiles.

### 2.2 Magnetosphere

We adopt the magnetospherical accretion flow model of Hartmann et al. (1994), as done by Muzerolle et al. (2001) and by Symington, Harries, & Kurosawa (2005a), in which the gas accretion on to the stellar surface from the innermost part of the accretion disc occurs through a dipolar stellar magnetic field. The magnetic field is assumed to be so strong that the gas flow does not affect the underlying magnetic field itself. As shown in Fig. 1, the innermost radius ( $R_{\text{mi}}$ ) of the magnetosphere at the equatorial plane ( $z = 0$ ) is assigned to be same as the inner radius ( $R_{\text{di}}$ ) of the accretion disc where the flow is truncated. In our models,  $R_{\text{mi}}$  and the outer radius

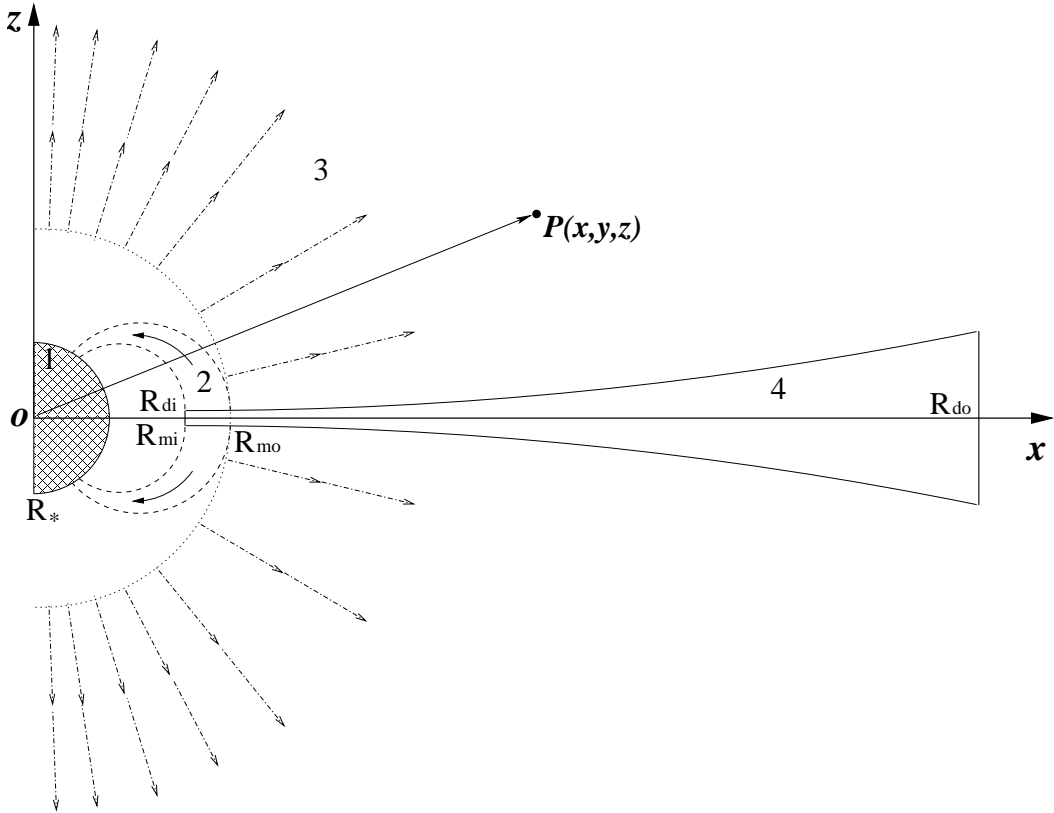


**Figure 1.** The basic model configuration. The system consists of four components: (1) the continuum source located at the origin ( $o$ ) of the cartesian coordinates ( $x, y, z$ ) – the  $y$ -axis are into the paper, (2) the magnetospherical accretion flow, (3) the bipolar wind outflow, and (4) the accretion disc. The density distribution is symmetric around the  $z$ -axis. The innermost radius of the magnetosphere (at the equatorial plane) coincides with the inner radius of the accretion disc. From the innermost part of the accretion disc, the gas falls freely, moving along the magnetic field onto the surface of the star. The bipolar wind starts from just outside of the largest radius ( $R_{mo}$ ) of the magnetosphere (dotted line).

**Table 1.** Summary of the standard classical T Tauri star model parameters.

Parameters	$R_*$ [ $R_\odot$ ]	$M_*$ [ $M_\odot$ ]	$T_{ph}$ [K]	$R_{mi}$ [ $R_*$ ]	$R_{mo}$ [ $R_*$ ]	$\dot{M}_{acc}$ [ $M_\odot \text{ yr}^{-1}$ ]	$\dot{M}_{wind}$ [ $M_\odot \text{ yr}^{-1}$ ]	$v_\infty$ [ $\text{km s}^{-1}$ ]	$b$ [-]	$R_{di}$ [ $R_*$ ]	$R_{do}$ [au]
Standard	2.0	0.5	4000	2.2	3.0	$10^{-7}$	$10^{-8}$	210	4.0	2.2	100

( $R_{mo}$ ) of the magnetosphere (at the equatorial plane) are set to be  $2.2 R_\odot$  and  $3.0 R_\odot$  respectively. The former value corresponds to the co-rotation radius of the accretion disc, and the geometry of the magnetic field/stream lines is kept constant throughout this paper. The geometry of the magnetosphere is identical to the “small/wide” model of Muzerolle et al. (2001).

The magnetic field and the gas stream lines are assumed to have the following simple form:

$$r = R_m \sin^2 \theta \quad (1)$$

(see Ghosh, Pethick, & Lamb 1977) where  $r$ , and  $\theta$  are coordinates of the field point ( $p$ ) in Fig. 1 in spherical coordinates, and  $R_m$  is the radial distance to the field line at the equatorial plane ( $\theta = \pi/2$ ). The range of  $R_m$  is restricted between  $R_{mi}$  and  $R_{mo}$ . Using the field geometry above and the conservation of energy, the velocity and the density of the accreting gas along the steam line are found as in Hartmann et al. (1994).

The temperature structure of the magnetospheric used by

Hartmann et al. (1994) is simply adopted here. They computed the temperature assuming a volumetric heating rate which is proportional to  $r^{-3}$ , and using the energy balance of the radiative cooling rate of Hartmann et al. (1982) and the heating rate (Hartmann et al. 1994). Although the temperature structure of the accretion steam could significantly affect the line source function, for the purpose of the exploring the general characteristics of the H $\alpha$  formation, this simple form is a reasonable assumption. Martin (1996) presented the self-consistent determination of the thermal structure of the inflowing gas along the dipole magnetic field (equation 1) by solving the heat equation couple to rate equations for hydrogen. He found that main heat source is adiabatic compression due to the converging nature of the flow, and the major contributors to the cooling process are bremsstrahlung radiation and line emission from Ca II and Mg II ions. The results of Martin (1996) qualitatively agree with that of Hartmann et al. (1994).

### 2.3 Outflow geometries

Two different types of the wind configurations are considered: (1) the bipolar wind model which resembles the density structure of the MHD simulation by Krasnopol'sky et al. (2003) in *large scale* ( $\sim 100$  au), and (2) the disc-wind model which resembles the density of the same MHD simulation in *small scale* ( $\sim 10$  au). While the wind density is more concentrated toward the polar directions in (1), it is more concentrated toward the equatorial direction in (2). The following describes each model in details.

#### 2.3.1 Bipolar Wind

Similar to the simple wind model of Appenzeller et al. (2005), the following parametrisation of collimated bipolar wind (region 3 in Fig. 1) is adopted. The wind velocity field,  $\mathbf{v}_{\text{wind}}$ , consists of radial and azimuthal components which depend on the spherical coordinates  $r$  and  $\theta$ . The radial component  $v_r(r)$  is assumed to be in the classical beta-velocity law (c.f. Castor & Lamers 1979), and the azimuthal component  $v_\phi$  is assumed to be a constant fraction ( $\gamma$ ) of the Keplerian velocity for a given distance ( $w = \sqrt{x^2 + y^2}$ ) from the symmetry axis ( $z$ -axis), i.e.:

$$\mathbf{v}_{\text{wind}} = v_r \hat{\mathbf{r}} + v_\phi \hat{\phi} \quad (2)$$

where

$$v_r(r) = v_{r0} + (v_\infty - v_{r0}) \left(1 - \frac{R_{\text{mo}}}{r}\right)^\beta, \quad (3)$$

$$v_\phi(w) = \gamma \left(\frac{GM_*}{w}\right)^{1/2}, \quad (4)$$

Note that the base of the wind starts at  $r = R_{\text{mo}}$ . This is chosen so mainly for computational simplicity i.e. to avoid the overlap between the wind and the magnetosphere; however, see Matt & Pudritz (2005) for the possibility that wind originates from the stellar surface (restricted near the polar caps). The range of the polar angle for the wind is restricted to  $\theta > |\theta_{\text{disc}}|$  where  $\theta_{\text{disc}}$  is the opening angle of the accretion disc, to avoid the overlap.  $v_{r0}$  is the small radial velocity at the base of the wind ( $r = R_{\text{mo}}$ ). Normally,  $v_{r0} = 10 \text{ km s}^{-1}$  which is approximately equal to the thermal velocity of hydrogen with  $T = 7500 \text{ K}$ . Following Appenzeller et al. (2005),  $\gamma = 0.05$  is adopted. The dependency of  $v_r$  in polar direction ( $\theta = 0$ ) on the values of wind acceleration parameter  $\beta$  is shown in Figure 2. All other parameters describing the wind are fixed as the standard values given in Table 1.

Further, the density of the wind is assumed to be axisymmetric and separable in  $r$  and  $\theta$ ,

$$\rho(r, \theta) = P(r) F(\theta) \quad (5)$$

with

$$F(\theta) = n \cos^b \theta \quad (6)$$

where  $b$  is normally positive even number (for the density symmetric about the equatorial plane), and  $n$  is the angular normalisation constant. For  $b = 0$ , the wind is spherically symmetric except for the parts disrupted by the accretion disc. The larger the value of  $b$ , the higher the degree of the collimation. By integrating equation 6 over angles and normalising the integral to  $4\pi$ , one finds

$$n = \frac{1+b}{1-\cos^{1+b} \theta_{\text{wind}}}. \quad (7)$$

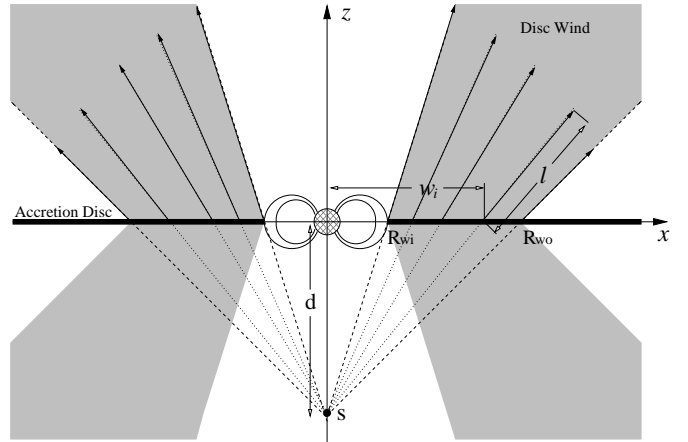


**Figure 3.** Basic model configuration of the disc-wind, magnetosphere hybrid model. The system consists of four components: (1) the continuum source located at the origin ( $o$ ) of the cartesian coordinates ( $x, y, z$ ) – the  $y$ -axis is into the paper, (2) the magnetospherical accretion flow, (3) the collimated wind/jet outflow, and (4) the geometrically thin (but opaque) accretion disc. The disc wind originates from the disc surface between  $w_i = R_{wi}$  and  $w_o = R_{wo}$ . The wind source points ( $S$ ), from which the stream lines diverge, are placed at distance  $d$  above and below the star. By changing the value of  $d$ , the degree of the wind collimation is controlled. The density distribution is symmetric around the  $z$ -axis.

Assuming the total mass-loss rate by the wind/jet is  $\dot{M}_{\text{wind}}$  and the mass-flux conserves in time, the radial part of the density function is reduced to  $P(r) = \dot{M}_{\text{wind}} [4\pi r^2 v_r(r)]^{-1}$ ; hence, Equation 5 becomes

$$\rho(r, \theta) = \frac{n \dot{M}_{\text{wind}} \cos^b \theta}{4\pi r^2 v_r(r)}. \quad (8)$$

For a given mass-accretion rate, the wind mass-loss rate in our typical model is assigned from the ratio of mass-loss to mass-accretion rate ( $\dot{M}_{\text{wind}}/\dot{M}_{\text{acc}} \approx 0.1$ ), indicated by both observations and MHD calculations (e.g. Königl & Pudritz 2000). Figure 2 shows the density along a streamline in the polar direction ( $\theta = 0$ ), for different values of  $\beta$  with all other parameters fixed as the standard values (Table 1). The density is relatively sensitive to the value of  $\beta$  for  $r < 10 R_{\text{mo}}$ , but a little difference is seen beyond  $r < 100 R_{\text{mo}}$ .

#### 2.3.2 Disc wind

The wind model presented here is intended to mimic the collimated MHD disc-wind calculations of Krasnopol'sky et al. (2003) in small scale ( $\sim 10$  au). Knigge, Woods, & Drew (1995) introduced the “split-monopole” kinematic disc-wind model in their studies of the UV resonance lines formed in the winds of cataclysmic variable stars. In this model, the outflow arises from the surface of the rotating accretion disc, and has a biconical geometry. The specific angular momentum is assumed to be conserved along a stream line, and the poloidal velocity component is assumed to be simply a radial from vertically displaced “sources” from the central star. We adopt their disc-wind model here, and consider the combined effect of the disc-wind and the magnetospherical accretion flow model described earlier. In the following, we briefly described their disc-wind model. For details of the models, readers are referred to Knigge et al. (1995) and Long & Knigge (2002).

Four basic parameters for the models are: (1) mass-loss rate, (2) the degree of the wind collimation, (3) the velocity gradients,

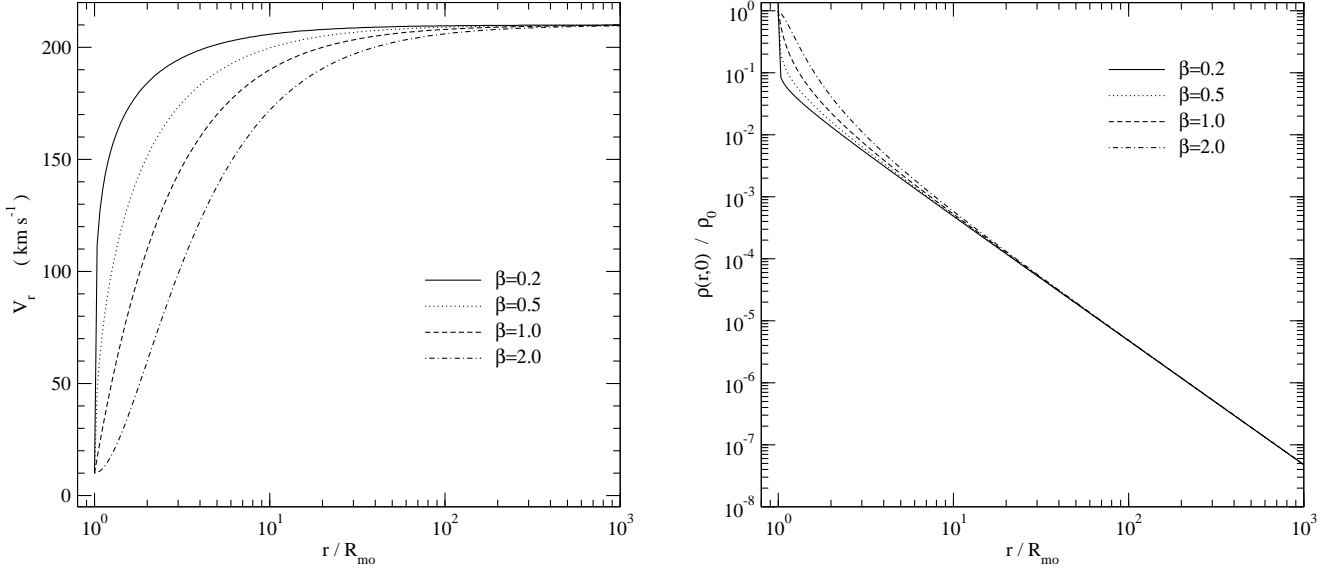


**Figure 2.** The dependency of the bipolar wind velocity and density structure on the wind acceleration parameter  $\beta$ . The radial component of the wind velocity (equation 3) in polar direction,  $\theta = 0$  as a function of radius is shown on the left. The wind density (equation 8) along polar direction as a function of radius is shown on the right. For all  $\beta$  values, the density is normalised to the density at the base of the wind in polar direction, i.e.  $\rho_0 = \rho(R_{\text{mo}}, 0)$ . The smaller the value of  $\beta$ , the faster the acceleration of the wind. For the radius ( $r/R_{\text{mo}} < 10$ , both velocity and density are sensitive to the value of  $\beta$ . For all  $\beta$  values, the radial velocity of the wind reaches the terminal velocity ( $\sim 210 \text{ km s}^{-1}$  by  $r/R_{\text{mo}} \sim 1000$ ). The initial velocity  $V_0 = 10 \text{ km s}^{-1}$ , which approximately corresponds to the thermal velocity of a hydrogen atom at 7500 K, is used for all  $v_r$  plots. Beyond  $r/R_{\text{mo}} = 100$ , little difference is seen in the polar density with different  $\beta$  values.

and (4) the wind temperature. The basic configuration of the disc-wind model is shown in Figure 3. The disc wind originates from the disc surface, but the ‘‘source’’ point ( $S$ ), from which the stream lines diverges, are placed at distance  $d$  above and below the centre of the star. By changing the value of  $d$ , the degree of the wind collimation is controlled. The larger the value of  $d$ , the wind becomes more parallel to the rotation axis, i.e. the wind becomes more collimated. The mass-loss launching is restricted between  $R_{\text{wi}}$  and  $R_{\text{wo}}$  where the former is set to be equal to the outer radius of the magnetosphere ( $R_{\text{mo}}$ ) for simplicity and the latter is set to 1 au as in Krasnopolsky et al. 2003.

The local mass-loss rate per unit area ( $\dot{m}$ ) is assumed to be proportional to the mid-plane temperature of the disc, and is a function of the cylindrical radius  $w = (x^2 + y^2)^{1/2}$ , i.e.

$$\dot{m}(w) \propto T(w)^\alpha. \quad (9)$$

Further, the mid-plane temperature of the disc is assumed to be expressed as a power-law in  $w$ ; thus,  $T \propto w^q$ . Using this in the relation above, one finds

$$\dot{m}(w) \propto w^p \quad (10)$$

where  $p = \alpha \times q$ . The index of the mid-plane temperature power law is adopted from the dust radiative transfer model of Whitney et al. (2003) who found the innermost part of the accretion disc has  $q = -1.15$ . To be consistent with the collimated disc-wind model of Krasnopolsky et al. (2003) who used  $p = -3/2$ , the value of  $\alpha$  is set to 1.3. The constant of proportionality in equation 10 is found by integrating  $\dot{m}$  from  $R_{\text{wi}}$  to  $R_{\text{wo}}$ , and the normalising the value to the total mass-loss rate  $\dot{M}_{\text{dw}}$ .

The azimuthal/rotational component of the wind velocity  $v_\phi(w, z)$  is computed from the Keplerian rotational velocity at the emerging point of the stream line i.e.  $v_\phi(w_i, 0) = (GM_*/w_i)^{1/2}$  where  $w_i$  is the distance from the rotational axis ( $z$ ) to the emerging

point on the disc, and by assuming the conservation of the specific angular momentum along a stream line:

$$v_\phi(w, z) = v_\phi(w_i, 0) \left( \frac{w_i}{w} \right). \quad (11)$$

Based on the classic  $\beta$  velocity law of hot stellar winds (c.f. Castor, Abbott, & Klein 1975), the poloidal component of the wind velocity ( $v_p$ ) parameterised as:

$$v_p(w_i, l) = c_s(w_i) + [f v_{\text{esc}} - c_s(w_i)] \left( 1 - \frac{R_s}{l + R_s} \right)^\beta \quad (12)$$

where  $c_s$ ,  $f$ , and  $l$  are the sound speed at the wind launching point on the disc, the constant scale factor of the asymptotic terminal velocity to the local escape velocity (from the wind emerging point on the disc), and the distance from the disc surface along stream lines respectively.  $R_s$  is the wind scale length, and  $R_s = 10 R_{\text{mi}}$  is adopted as similarly done by Long & Knigge (2002).

Assuming the mass-flux conservation and using the velocity field defined above, the disc wind density as a function of  $w$  and  $l$  can be written as

$$\rho(w_i, l) = \frac{\dot{m}(w_i)}{v_p(w_i, l) |\cos \delta|} \left\{ \frac{d}{Q(w_i, l) \cos \delta} \right\}^2 \quad (13)$$

where  $Q$  and  $\delta$  are the distance from the source point ( $S$ ) to a point along the stream line and the angle between the stream line and the disc normal respectively. Figure 4 shows the density and the velocity components along the mid stream line (passing through  $w_i = (R_{\text{wi}} + R_{\text{wo}})/2$  on the disc plane ( $z = 0$ ) for different values of the wind acceleration parameter  $\beta$ .

## 2.4 Accretion disc

Although it is possible, in our model, to compute the dust-sublimation radius and the vertical hydrostatic structure of the ac-

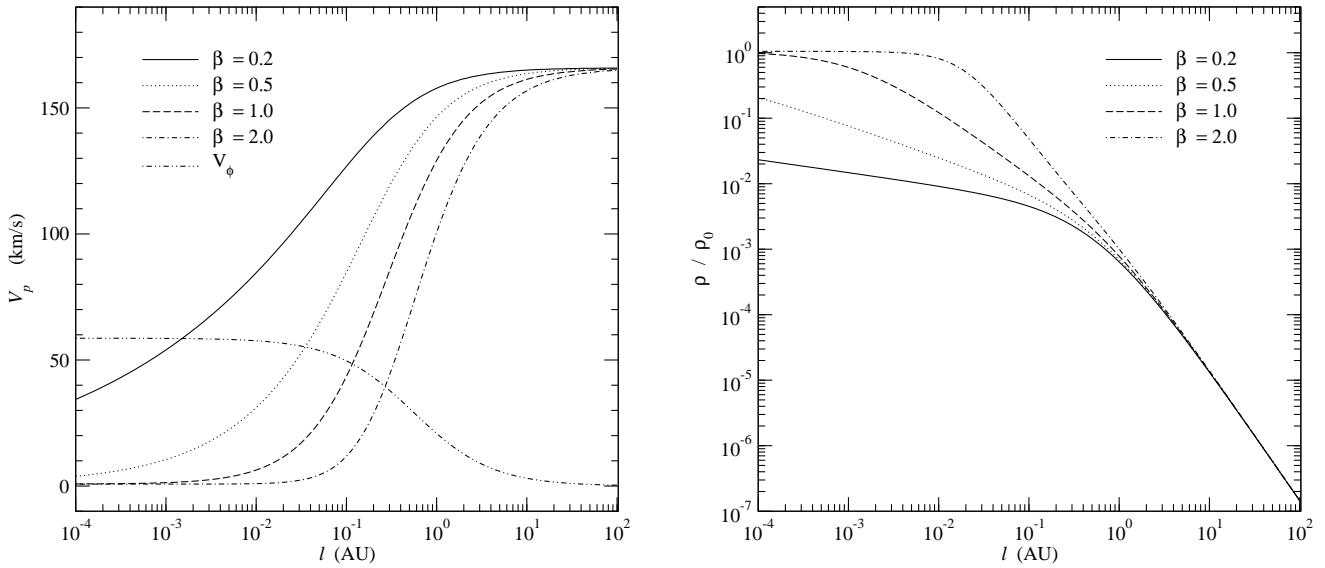


**Figure 4.** Dependency of the disc-wind density and velocity on the wind acceleration parameter  $\beta$ . The wind density  $\rho$  (left panel) and the poloidal velocity component  $V_p$  (right panel) along the stream line starting from the mid point of the wind launching zone, i.e.  $(w, z) = (w_{\text{mid}}, 0)$  where  $w_{\text{mid}} = (R_{\text{wi}} + R_{\text{wo}})/2$ , are shown as a function of the distance ( $l$ ) from the wind launching point (c.f. equations 12 and 13). The azimuthal velocity component ( $V_\phi$ ), which is independent of  $\beta$  (c.f. equation 11), is also shown in the right panel for a comparison. The density is normalised to the density  $\rho_0$  at the wind launching point for  $\beta = 1.0$  case. The  $V_p$  reaches the terminal velocity by 100 au for all  $\beta$ . In the far field ( $l > 10$  au), the density is approximately proportional to  $\sim l^2$ . Up to  $l \sim 10$  au, the density is smaller and the poloidal speed is larger for the wind with a larger  $\beta$  value.

cretion disc self-consistently (assuming the radial dependency of the mid-plane density) by using an iterative Monte Carlo radiative transfer technique (c.f. Walker et al. 2004), we find it to be too time consuming for the purpose of this paper – understanding the general characteristic of H $\alpha$  profile shapes hence exploring a large parameter space. For this reason, we adopt a simple analytical disc model, the steady  $\alpha$ -disc ‘standard model’ (Shakura & Sunyaev 1973; Frank, King, & Raine 2002) with the inner radius fixed at the inner radius of the magnetosphere at equatorial plane. This corresponds to Region 4 in Fig. 1.

#### 2.4.1 Density and velocity

The disc density distribution is given by

$$\rho_d(w, z) = \Sigma(w) \frac{1}{\sqrt{2\pi} h(w)} e^{-\left(\frac{z}{2h(w)}\right)^2} \quad (14)$$

where  $w = \sqrt{x^2 + y^2}$ ,  $h$ ,  $z$  and  $\Sigma$  are the distance from the symmetry axis, the scale height, the distance from the disc plane, and the surface density at the mid-plane, respectively. The mid-plane surface density and the scale height are given as:

$$\Sigma(w) = \frac{5M_d}{8\pi R_{\text{do}}^2} w^{-3/4} \quad (15)$$

where  $R_{\text{do}}$  and  $M_d$  are the disc radius and the disc mass respectively.

$$h(w) = 0.05 R_{\text{do}} w^{9/8}. \quad (16)$$

With these parameters, the disc is slightly flared. The inner radius of the disc is set to  $R_{\text{di}} = R_{\text{mi}}$  (the inner radius of the magnetosphere at the equatorial plane), which is approximately same as the co-rotating radius of the system with the parameters in Table 1. The disc mass,  $M_d$ , of an object is assumed to be 1/100 of the central

mass ( $M_*$ ), and the disc radius ( $R_{\text{di}}$ ) to be 100 au. The velocity of the gas/dust in the disc is assumed to be Keplerian.

#### 2.4.2 Dust model

To calculate the dust scattering and absorption cross section as a function of wavelength, the optical constants of Draine & Lee (1984) for amorphous carbon grains and Hanner (1988) for silicate grains are used. The model uses the “large grain” dust model of Wood et al. (2002) in which the dust grain size distribution is described by the following function:

$$n(a) da = (C_C + C_{\text{Si}}) a^{-p} \exp\left[-\left(\frac{a}{a_c}\right)^q\right] da \quad (17)$$

where  $a$  is the grain size restricted between  $a_{\text{min}}$  and  $a_{\text{max}}$ , and  $C_C$  and  $C_{\text{Si}}$  are the terms set by requiring the grains to completely deplete a solar abundance carbon and silicon. The parameters adopted in our model are:  $C_C = 1.32 \times 10^{-17}$ ,  $C_{\text{Si}} = 1.05 \times 10^{-17}$ ,  $p = 3.0$ ,  $q = 0.6$ ,  $a_{\text{min}} = 0.1 \mu\text{m}$ ,  $a_{\text{max}} = 1000 \mu\text{m}$ , and  $a_c = 50 \mu\text{m}$ . This corresponds to Model 1 of the dust model used by Wood et al. (2002). See also their Fig. 3. The relative number of each grain is assumed to be that of solar abundance, C/H  $\sim 3.5 \times 10^{-4}$  (Anders & Grevesse 1989) and Si/H  $\sim 3.6 \times 10^{-5}$  (Grevesse & Noels 1993) which are similar to values found in the ISM model of Mathis, Rumpl, & Nordsieck (1977) and Kim, Martin, & Hendry (1994). Similar abundances were used in the circumstellar disc models of Cotera et al. (2001).

## 3 RADIATIVE TRANSFER MODEL

We have extended the TORUS radiative transfer code (Harries 2000; Kurosawa et al. 2004; Symington et al. 2005a) to compute the H $\alpha$  profiles from pre-main-sequence stars which are surrounded

by one or more of the following: the magnetospherical accretion flow, the out-flowing collimated wind, and the accretion disc. Previously in Symington et al. (2005a), the model used in the three-dimensional (3-D) adaptive mesh refinement (AMR) to investigate the line variability mainly associated with rotational motion of complex geometrical configurations of magnetospherical flow (see also Kurosawa, Harries, & Symington 2005). We modified the code to handle the two-dimensional (2-D) density distribution, and restricted our models to be axi-symmetric. It was done in order to enable us to explore rather large number of parameters (c.f. section 2). Note that the velocity field is still in 3-D – the third component can be calculated by using the symmetry for a given value of azimuthal angle. An examples of how the AMR grid for the purpose of the radiative transfer is constructed are presented in e.g. Wolf, Henning, & Stecklum (1999), Kurosawa & Hillier (2001), Steinacker et al. (2003) and Kurosawa et al. (2004).

The computation of H $\alpha$  is divided in two parts: (1) the source function calculation ( $S_\nu$ ) and (2) the observed flux/profile calculation. In the first process, we have utilised the method by Klein & Castor (1978) (see also Rybicki & Hummer 1978; Hartmann et al. 1994) in which the Sobolev approximation method is applied. The population of the bound states of hydrogen are assumed to be in statistical equilibrium, and the gas to be in radiative equilibrium. Our hydrogen atom model consist of 14 bound state and continuum. Readers are refer to Harries (2000) for details.

To compute the observed line profile, the Monte Carlo radiative transfer method (e.g. Hillier 1991) using the Sobolev escape-probability can be used when (1) a large velocity gradient is present in the gas flow, and (2) the intrinsic line width is negligible compared to the Doppler broadening of the line. In our earlier models (Harries 2000; Symington et al. 2005a), this method was used to compute the line profiles since the condition (1) and (2) are reasonably satisfied. However, as noted and demonstrated by Muzerolle et al. (2001), even with a moderate amount of mass-accretion rate ( $10^{-7} M_\odot \text{ yr}^{-1}$ ), Stark broadening becomes important in the optically thick H $\alpha$  line. Muzerolle et al. (2001) also pointed out that the observed H $\alpha$  profiles from CTTS typically have the wings extending to  $500 \text{ km s}^{-1}$  (e.g. Edwards et al. 1994; Reipurth et al. 1996) which cannot be explained by the infall velocity of the gas along the magnetosphere alone.

To implement the broadening mechanism into our previous model (Symington et al. 2005a), we follow the formalism adopted by Muzerolle et al. (2001). First, the emission and absorption profiles are replaced from the Doppler to the Voigt profile, which is defined as:

$$H(a, y) \equiv \frac{a}{\pi} \int_{-\infty}^{\infty} \frac{e^{-y'^2}}{(y - y')^2 + a^2} dy' \quad (18)$$

where  $a = \Gamma/4\pi\Delta\nu_D$ ,  $y = (\nu - \nu_0)/\Delta\nu_D$ , and  $y' = (\nu' - \nu_0)/\Delta\nu_D$  (c.f. Mihalas 1978).  $\nu_0$  is the line centre frequency, and  $\Delta\nu_D$  is the Doppler line width of hydrogen atom (due to its thermal motion) which is given by  $\Delta\nu_D = (2kT/m_H)^{1/2} \times (\nu_0/c)$  where  $m_H$  is the mass of a hydrogen atom. The damping constant  $\Gamma$ , which depends on the physical condition of the gas, is parameterised by Vernazza, Avrett, & Loeser (1973) as follows:

$$\begin{aligned} \Gamma = & C_{\text{rad}} + C_{\text{vdW}} \left( \frac{n_{\text{HI}}}{10^{16} \text{ cm}^{-3}} \right) \left( \frac{T}{5000 \text{ K}} \right)^{0.3} \\ & + C_{\text{Stark}} \left( \frac{n_e}{10^{12} \text{ cm}^{-3}} \right)^{2/3} \end{aligned} \quad (19)$$

where  $n_{\text{HI}}$  and  $n_e$  are the number density of neutral hydrogens

and that of free electrons. Also,  $C_{\text{rad}}$ ,  $C_{\text{vdW}}$  and  $C_{\text{Stark}}$  are natural broadening, van der Waals broadening, and linear Stark broadening constants respectively. We simply adopt this parameterisation along with the values of broadening constants for H $\alpha$  from Luttermoser & Johnson (1992), i.e.  $C_{\text{rad}} = 6.5 \times 10^{-4} \text{ \AA}$ ,  $C_{\text{vdW}} = 4.4 \times 10^{-4} \text{ \AA}$  and  $C_{\text{Stark}} = 1.17 \times 10^{-3} \text{ \AA}$ . In terms of level populations and the Voigt profile, the line opacity for the transition  $i \rightarrow j$  can be written as:

$$\chi_l = \frac{\pi^{1/2} e^2}{m_e c} f_{ij} n_j \left( 1 - \frac{g_j n_i}{g_i n_j} \right) H(a, y) \quad (20)$$

where  $f_{ij}$ ,  $n_i$ ,  $n_j$ ,  $g_i$  and  $g_j$  are the oscillator strength, the population of  $i$ -th level, the population of  $j$ -th level, the degeneracy of the  $i$ -th level, and the degeneracy of the  $j$ -th level respectively.  $m_e$  and  $e$  are the electron mass and charge (c.f. Mihalas 1978).

The second modification in our model is the replacement of the method of solving the formal solution from the Monte Carlo radiative transfer method with Sobolev approximation to the direct integration method (c.f. Muzerolle et al. 2001). We specify the cylindrical coordinates  $(p, q, t)$  which is the original stellar coordinate system  $(\rho, \phi, z)$  rotated (around  $y$  axis) by the inclination of the line of sight, i.e. the  $t$ -axis coincides with the line of sight. The observed flux ( $F_\nu$ ) is given by:

$$F_\nu = \frac{1}{4\pi d^2} \int_0^{p_{\max}} \int_0^{2\pi} p \sin q I_\nu dq dp \quad (21)$$

where  $d$ ,  $p_{\max}$ , and  $I_\nu$  are the distance to an observer, the maximum extent to the model space in the projected (rotated) plane, and the specific intensity ( $I_\nu$ ) in the direction on observer at the outer boundary. For a given ray along  $t$ , the specific intensity is given by:

$$I_\nu = I_0 e^{-\tau_\infty} + \int_{t_0}^{t_\infty} S_\nu(t) e^{-\tau} dt \quad (22)$$

where  $I_0$  and  $S_\nu$  are the intensity at the boundary on the opposite to the observer and the source function ( $\eta_\nu/\chi_\nu$ ) of the stellar atmosphere/wind at a frequency  $\nu$ . For a ray which intersects with the stellar core,  $I_0$  is computed from the stellar atmosphere model of Kurucz (1979) as described in section 2.1, and  $I_0 = 0$  otherwise. The initial position of each ray is assigned to be at the centre of the surface element ( $dA = p \sin q dq dp$ ). The code execution time is proportional to  $n_p n_q n_\nu$  where  $n_p$  and  $n_q$  are the number of cylindrical radial and angular points for the flux integration, and  $n_\nu$  is the number of frequency points. In the models presented in the following section,  $n_p = 180$ ,  $n_q = 100$ , and  $n_\nu = 101$  are used unless specified otherwise. A linearly spaced radial grid is used for the area where the ray intersects with magnetosphere, and a logarithmically spaced grid is used for the wind and the accretion disc regions.

The optical depth  $\tau$  is equation 22 is defined as:

$$\tau(t) \equiv \int_t^\infty \chi_\nu(t') dt'$$

where  $\chi_\nu$  is the opacity of media the ray passes through.  $\tau_\infty$  is the total optical depth measured from the initial ray point to the observer (or to the outer boundary closer to the observer). Initially, the optical depth segments  $d\tau$  are computed at the intersections of a ray with the original AMR grid in which the opacity and emissivity information are stored. For high optical depth models, additional points are inserted between the original points along the ray, and  $\eta_\nu$  are  $\chi_\nu$  values are interpolated to those points to ensure  $d\tau < 0.05$  for the all ray segments.

For a point in the magnetosphere and the wind flows, the emissivity and the opacity of the media are given as:

$$\begin{cases} \eta_\nu &= \eta_c^H + \eta_l^H \\ \chi_\nu &= \chi_c^H + \chi_l^H + \sigma_{\text{es}} \end{cases} \quad (23)$$

where  $\eta_c^H$  and  $\eta_l^H$  are the continuum and line emissivity of hydrogen.  $\chi_c^H$ ,  $\chi_l^H$ , and  $\sigma_{\text{es}}$  are the continuum, line opacity (equation 20) of hydrogen, and the electron scattering opacity. Similarly, for a point in the accretion disc,

$$\begin{cases} \eta_\nu &= 0 \\ \chi_\nu &= \kappa_{\text{abs}}^{\text{dust}} + \kappa_{\text{sca}}^{\text{dust}} \end{cases} \quad (24)$$

where  $\kappa_{\text{abs}}^{\text{dust}}$  and  $\kappa_{\text{sca}}^{\text{dust}}$  are the dust absorption, and scattering opacity which are calculated using the dust property described in section 17. For computational simplicity, we assumed that the dust emissivity is zero. Since the disc mass of CTTS are rather small ( $\sim 0.01 M_\odot$ ) and low temperature ( $<\sim 1600$  K), the continuum flux contribution at H $\alpha$  wavelength is expected to be negligible (e.g. Chiang & Goldreich 1997).

## 4 RESULTS

### 4.1 Magnetosphere

Using the standard parameters (Table 1) for the central star and the magnetosphere, we examine the dependency of H $\alpha$  on the temperature ( $T_{\text{max}}$ ) of accretion flow and the mass accretion rate ( $\dot{M}_{\text{acc}}$ ), as similarly done by Muzerolle et al. (2001) for H $\beta$ . The hot ring temperature is computed from the available kinetic energy of the free-falling gas as describe by Hartmann et al. (1994) while Muzerolle et al. (2001) used the constant hot ring temperature (8000 K) for most of their models. The accretion luminosity ( $L_{\text{acc}}$ ) of models with  $\dot{M}_{\text{acc}} = 10^{-7} M_\odot \text{ yr}^{-1}$  is about a half of the total luminosity (without the hot ring) of the star, and  $L_{\text{acc}}$  is proportional to  $\dot{M}_{\text{acc}}$ . The results are placed in Figure 5. Overall dependency on  $T_{\text{max}}$  and  $\dot{M}_{\text{acc}}$  are similar to that of Muzerolle et al. (2001). In general, the line strength becomes weaker as the accretion rate and the temperature become smaller. The red-shifted absorption becomes less visible for higher accretion rate and temperature models in which the flux in the damping wings become important. Figure 6 shows an example of the effect of the broadening of H alpha (with  $T_{\text{max}} = 7500$  K and  $\dot{M}_{\text{acc}} = 10^{-7} M_\odot \text{ yr}^{-1}$ ) due to the damping constants as described in section 3. Although the maximum flux of the model with the broadening is almost identical to that of the model with no damping constant ( $\Gamma = 0$ ), a significant increase of the line flux in both red and blue wings of seen in the model with broadening. The weak red-shifted absorption component (which is a signature of the magnetospherical accretion) is weakened or eliminated by the flux in broadened wing.

Table 2 shows the EW for the models shown in Figure 5. About a half of the models shown the figure agree with the observed EW values of H $\alpha$  from 30 TTS presented by Alencar & Basri (2000) who found the EW of H $\alpha$  ranges from  $\sim 3$  Å to  $\sim 160$  Å, and the mean to be  $\sim 55$  Å. For the lowest  $\dot{M}_{\text{acc}}$  models, the EW values are smaller than the minimum EW observed by Alencar & Basri (2000), and for some models the EWs are negative. Since the target selection criteria of Alencar & Basri (2000) is not stated in their paper, we can not conclude that these low  $\dot{M}_{\text{acc}}$  models disagree with the observation. Reipurth et al. (1996), who measured the EW of 43 TTS and found similar distribution of EW values, mentioned that their EW measurements are under-representing real samples since the selection of the targets are based on the strong emission in H $\alpha$  surveys.

The dependency of the profile on the inclination angle ( $i$ ) is

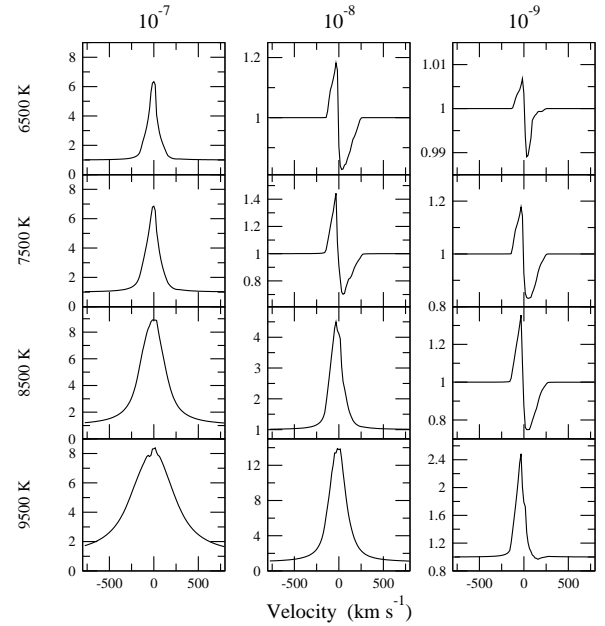


**Figure 5.** H $\alpha$  model profiles for wide ranges of mass accretion rate ( $\dot{M}_{\text{acc}}$ ) and temperature ( $T_{\text{max}}$ ). The profiles are computed using only magnetospherical accretion flow (i.e. no wind/jet). All the profiles are computed using the parameters of the ‘standard’ model (Table 1) and inclination  $i = 55^\circ$ . The temperature (indicated along the vertical axis) of the model increase from top to bottom, and the mass accretion rate (indicated by the values in  $M_\odot \text{ yr}^{-1}$  at the top) increases from left to right. The profiles are similar to those of Muzerolle et al. (2001), available on-line ([http://cfa-www.harvard.edu/cfa/youngstars/models/magnetospheric\\_models.html](http://cfa-www.harvard.edu/cfa/youngstars/models/magnetospheric_models.html)).

demonstrated in Figure 7. The model uses the same parameters as in Figure 6 (with broadening,  $T_{\text{max}} = 7500$  K and  $\dot{M}_{\text{acc}} = 10^{-7} M_\odot \text{ yr}^{-1}$ ). The figure shows that the peak (normalised) flux decreases as the inclination angle increases. Similarly, the equivalent width also decreases as the inclination increases. Because of the geometry of the magnetospherical accretion (c.f. Figure 1) and of the presence of the gas with the highest velocity close to the stellar surface, the highest red-shifted line-of-sight velocity is visible only at the high inclination angles. This explains the wider appearance of the profile with  $i = 80^\circ$  compared to the relatively narrow line appearance of the profile with  $i = 10^\circ$ . Although not shown here, a similar dependency on the inclination angle is found for the models with different temperatures ( $T_{\text{max}} = 6500, 8500, 9500$  K).

As seen in the models of Hartmann et al. (1994) and Muzerolle et al. (2001), our models also show the blue-shifted peak and the blue-ward asymmetry caused by the occultation of the accretion flow by the equatorial disc and the stellar disc. However, Alencar & Basri 2000 (see their Fig. 9) found a substantial fraction of the observed H $\alpha$  profiles also shows the “red-shifted” peak, and the P Cygni profiles which can not be explained by the magnetospherical accretion model alone. In addition, a recent study by Appenzeller et al. (2005) showed that the equivalent width of H $\alpha$  from CTTS increases as the inclination angle increases. Our model with the magnetospherical accretion flow clearly disagrees with their finding.

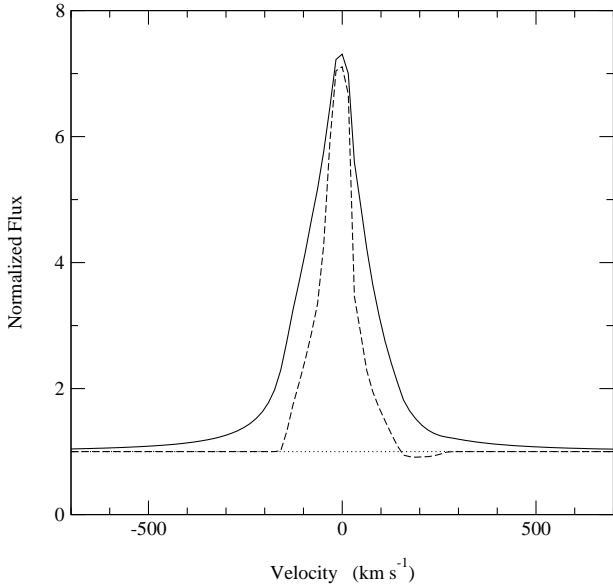


**Figure 6.** The effect of line broadening for H $\alpha$ . The model computed with a damping constant ( $\Gamma$ ), described in section 3 (solid), is compared with the model with no damping,  $\Gamma = 0$  (dashed). Both models are computed with  $T_{\max} = 7500$  K,  $i = 55^\circ$ , and the standard parameters given in Table 1. The two models have similar peak flux levels (around  $V \sim 0$  km s $^{-1}$ ), but the total flux and the EW of the line increased drastically for the model with the damping constant. The broad wings extend to  $\sim \pm 800$  km s $^{-1}$ . The redshifted absorption feature (very weakly) seen in the  $\Gamma = 0$  model is not seen in the model with the broadening.

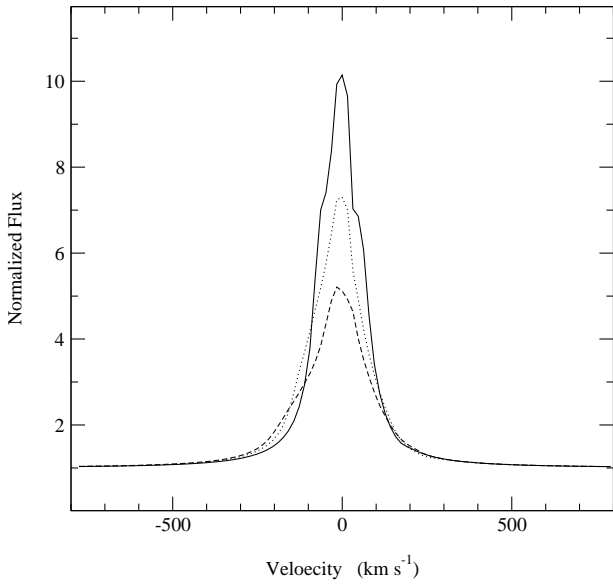


**Figure 7.** Dependency of H $\alpha$  profiles on inclination ( $i$ ). The profiles are computed with the magnetospherical accretion flow using the standard parameters given in Table 1 and  $T_{\max} = 7500$  K. The solid, dotted, and dashed lines are for  $i = 10^\circ$ ,  $55^\circ$ , and  $80^\circ$  respectively. As the inclination becomes larger, the peak flux and the equivalent width of the line becomes smaller. Similar dependency is seen in the models with the wide ranges of  $T_{\max}$  and  $\beta$ .

**Table 2.** Summary of H $\alpha$  equivalent widths from the magnetospherical accretion flow models shown in Figure 5.

$T_{\max}$ (K)	$\dot{M}_{\text{acc}}$ ( $M_{\odot}$ yr $^{-1}$ )		
	$10^{-7}$	$10^{-8}$	$10^{-9}$
6500	17.9	0.1	0.0
7500	25.2	-0.9	-0.5
8500	68.3	6.5	-0.7
9500	98.6	52.4	1.3

## 4.2 Bipolar Wind

As mentioned earlier, the magnetospherical accretion flow model alone cannot explain some of the features seen in observations. As an alternative model, we now examine formation of H $\alpha$  in a simple bipolar wind as described in section 2.3.1. The basic wind model parameters introduced earlier are  $\gamma$ ,  $\beta$ ,  $v_{\infty}$ ,  $b$ ,  $\theta_{\text{wind}}$ ,  $T_{\text{wind}}$  and  $\dot{M}_{\text{wind}}$ . To minimise the number of free parameters, we initially adopt  $\gamma = 0.05$ ,  $v_{\infty} = 210$  km s $^{-1}$  (Appenzeller et al. 2005) and  $\dot{M}_{\text{wind}} = 10^{-8} M_{\odot}$  yr $^{-1}$ . Further, the angular extent of the wind (the opening angle of the wind) is assumed to be  $\theta_{\text{wind}} = 80^\circ$ . The degree of collimation is initially chosen to be  $b = 4$ , i.e. the ratio of the density in polar direction to the density at the edge of the wind closest to the accretion disc is about  $(\cos 0^\circ / \cos 80^\circ)^4 \approx 10^3$ , for given radii. For simplicity, the wind temperature  $T_{\text{wind}}$  is assumed to be isothermal. Although the line is potentially sensitive to the temperature structure of the wind, determination of a self-consistent wind temperature is beyond the scope of this paper. Readers are referred to Hartmann et al. (1982) in which the wind temperature structure is determined by balancing the radiative cooling rate (assuming optically thin) with the MHD wave heating rate. With these parameters kept constant, we examine the characteristics of H $\alpha$  profiles, as a function of the wind acceleration parameter  $\beta$  and the isothermal wind temperature  $T_{\text{wind}}$ . Dependency on the other parameters will be discussed later in this section.

Figure 8 shows the profile computed at a mid inclination angle  $i = 55^\circ$  for the range of the wind temperature between 7000 K and 9000 K, and for the range of  $\beta$  between 0.2 and 2.0. The P Cygni profiles are prominent in the models with lower values of  $T_{\text{wind}}$  and  $\beta$  (colder and faster acceleration wind). As the value of  $\beta$  increases, the position of the blue-shifted absorption component moves toward the line centre, which can be seen clearly in the  $T_{\text{wind}} = 7000$  K models. While the velocity position of absorption component for the fastest acceleration ( $\beta = 0.2$ ) is almost at the terminal velocity ( $v_{\infty} \sim 210$  km s $^{-1}$ ), that for the slowest wind acceleration model ( $\beta = 4.0$ ) is located close to the line centre ( $\sim 50$  km s $^{-1}$ ). As one can see in Figure 2, the column density of the gas moving at  $v_{\infty}$  increases as the wind acceleration becomes larger since the gas moving at  $v_{\infty}$  becomes closer to the photosphere. At the location where the absorption occurs, the gas is moving faster for the models with the faster wind acceleration models; hence, the location of the absorption component is bluer as  $\beta$  becomes smaller (as the wind acceleration faster). The figure also shows that the intensity of the emission component increases as  $\beta$  increases for a given  $T_{\text{wind}}$ . This is mainly because the density near the photosphere increases as the value of  $\beta$  increases (Figure 2); hence, the emissivity of increases. Unlike the magnetospherical accretion only models (Figure 5), the inverse P Cygni profiles are not seen here, nor the blue-ward asymmetry. Because of the absorption component in P Cygni profile, most of the profiles show red-ward

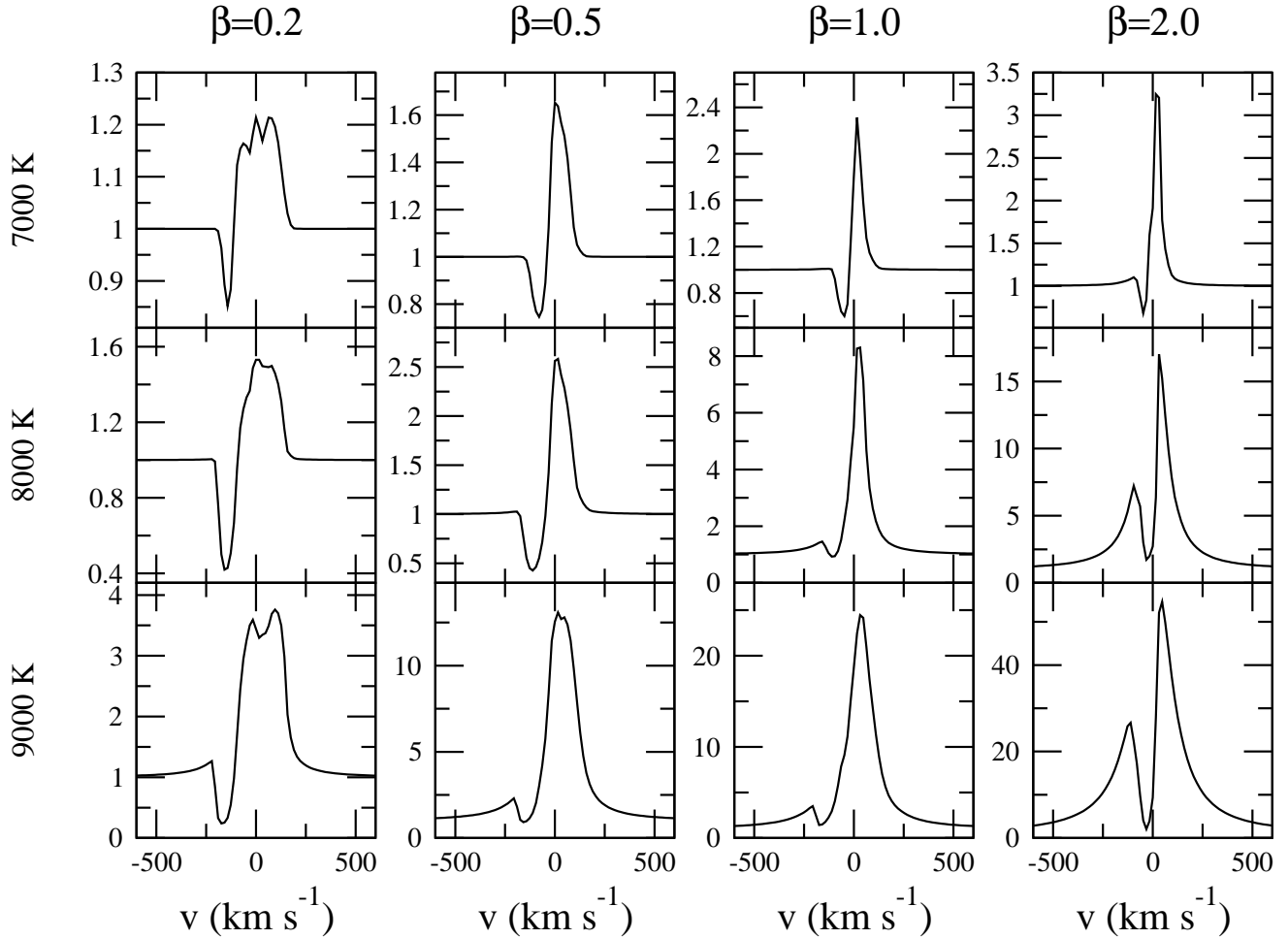


**Figure 8.** H $\alpha$  model profiles computed with wide ranges of the isothermal wind temperature ( $T_{\text{wind}}$ ) and the wind acceleration rate ( $\beta$ ). The profiles are computed with the wind component only (no magnetospherical accretion flow or accretion disc). The ‘standard’ model parameters (Table 1) are applied. The wind mass-loss rate ( $\dot{M}_{\text{wind}}$ ), the inclination ( $i$ ) and the degree of columnniation ( $b$ ) are fixed at  $10^{-8} M_{\odot} \text{ yr}^{-1}$ ,  $55^\circ$  and 4.0 respectively. The temperature (indicated along the vertical axis) of the model increases from top to bottom, and the wind acceleration rate increases from left to right. The P Cygni profile are seen for lower  $T_{\text{wind}}$  and lower  $\beta$  (slow acceleration) models. The position of the absorption the component moves toward the line centre as  $\beta$  increases. The effect of line broadening becomes more prominent for higher  $T_{\text{wind}}$  and higher  $\beta$  models.

asymmetry except for the low temperature wind models with high inclinations (not shown here).

The dependency of the profile on the wind anisotropy parameter  $b$  is demonstrated in Figure 9. Three models presented in the figure have the same mass-loss rate ( $10^{-8} M_{\odot} \text{ yr}^{-1}$ ), and are computed at inclination angle  $i = 55^\circ$ . The P Cygni profile feature becomes more prominent, and the line flux becomes smaller as the wind becomes more isotropic (smaller  $b$  value). For a fixed mass-loss rate, the column density of along the line of a sight to the observer at a medium inclination angle (e.g.  $i = 55^\circ$ ) increases as  $b$  decreases (c.f. equation 8); hence, causing more absorption. Further more, the value of the highest density in the wind becomes smaller for a smaller  $b$  model. As the wind becomes more isotropic, the material in the polar direction has to be spread in the wider angular angles. This results in a smaller highest density region in the wind; hence the smaller line emissivity. For the same reason, the emission in the wings is weaker for the model smaller  $b$  value. We also note that the asymmetry around the line centre decreases as the wind becomes more isotropic.

The effect of varying the wind mass-loss rate is shown in Fig-

ure 10. The line is very sensitive to the mass-loss rate. With all other parameters fixed constant,  $\dot{M}_{\text{wind}}$  acts as an scaling factor of the wind density (equation 8). The important processes in forming H $\alpha$  emission are the recombination process and the subsequent downward transition to  $n = 3$  level. Assuming the ionisation fraction remains constant, the recombination rate is proportional to the square of wind density. We have found the line flux of the models in the figure is approximately proportional to the square of the mass-loss rate. This very sensitive nature of H $\alpha$  would make the line a good candidate for a mass-loss rate indicator; however, without solving the ambiguity of the emission component from the magnetospherical accretion flow and the wind, and without knowing the detailed temperature structure of the wind, it could provide us a misleading a mass-loss rate estimate of a T Tauri star.

#### 4.3 Disc +bipolar wind

Next, we examine the effect of the size of the inner radius of the disc and the distribution of the H $\alpha$  emission region. Figure 11 shows the wind emission profiles computed with and without the

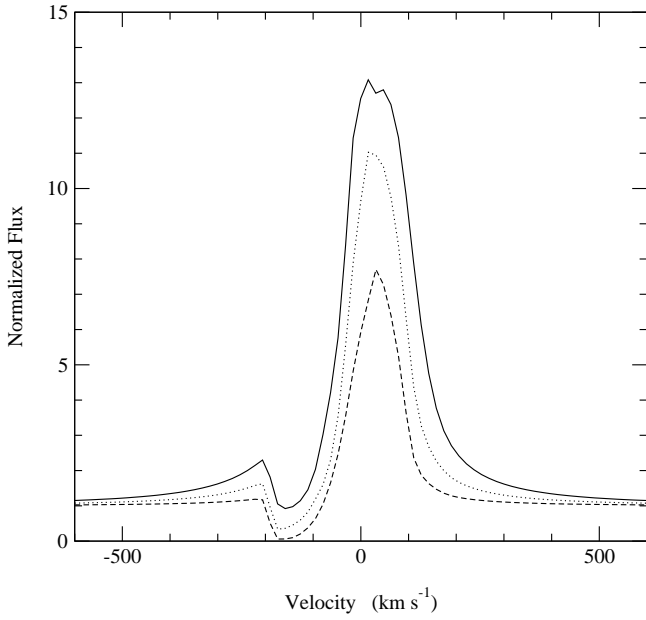


**Figure 9.** The effect of wind collimation. The line profiles computed with  $(T_{\text{wind}}, \beta) = (9000\text{K}, 0.5)$  for the wind anisotropy parameter  $b = 0, 2, 4$  are shown in dashed, dotted, and solid respectively. All the other parameters are same as in Figure 8. The P Cygni profile feature becomes prominent for the spherical wind model since the column density of along the line of a sight of the observer at a mid inclination angle ( $i = 55^\circ$ ) increases for lower  $b$  values for a fixed mass-loss rate of the wind. The blue-ward asymmetry is still present even in the isotropic wind case ( $b = 0$ ).

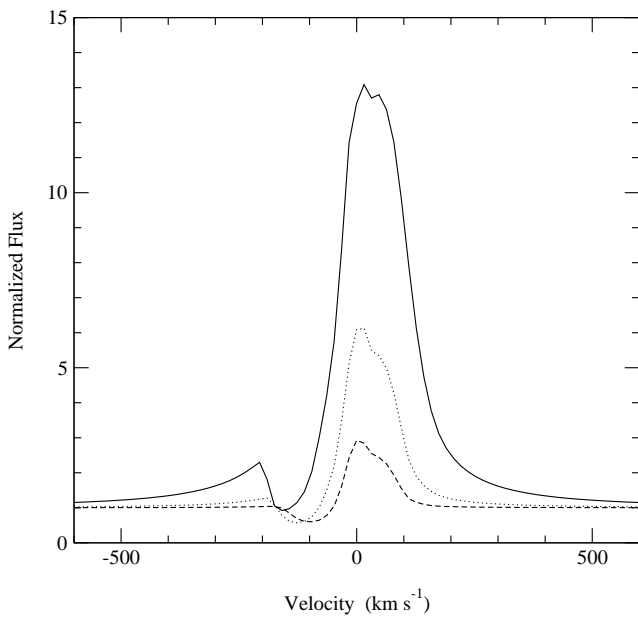


**Figure 10.** The effect of the wind mass-loss rate. The profiles computed with  $(T_{\text{wind}}, \beta) = (9000\text{K}, 0.5)$ , and  $\dot{M}_{\text{wind}} = 1.0 \times 10^{-8} \text{M}_\odot \text{yr}^{-1}$  (solid),  $0.5 \times 10^{-8} \text{M}_\odot \text{yr}^{-1}$  (dotted), and  $0.25 \times 10^{-8} \text{M}_\odot \text{yr}^{-1}$  (dashed) are shown above. The models are computed with only the wind component (no magnetospherical accretion flow or accretion disc). With all other parameter fixed constant, the mass-loss rate behaves as a scaling factor for the wind density (equation 8).

accretion disc at  $i = 55^\circ$ . The H $\alpha$  images (projected on to the plane perpendicular to the observer at the location of the star) are also shown in the same figure. Both models use the same parameters as in Figure 8, but with  $\beta = 0.5$  and  $T_{\text{wind}} = 9000$  K. The model without the disc can be also considered as a model with a large inner radius of the accretion disc, in which none of the wind emission region is blocked by the disc — provided the inclination angle is not high and the disc is not or slightly flared.

The bipolar nature of the wind is clearly seen in the images. In this example, the most of the wind emission occurs within a few to a several (depending mainly on the value of  $\beta$ ) stellar radii from the star. The figure also shows that the accretion disc blocking the wind emission from the bottom half of the wind which is moving away from the observer. This results in the reduction of the wind emission in the red wing. The image (mid panel) also shows that the accretion disc is not occulting the stellar disc at this inclination; therefore, the ratio of the wind emission flux to the photospherical continuum flux becomes slightly smaller for the model with the disc. This results in the reduction in the peak flux and the flux in the wings in the normalised profile shape. If the disc becomes more flared (if the opening angle exceeds  $45^\circ$  at the outer edge of the accretion disc), the occultation of the stellar disc by the accretion disc could be seen at this inclination angle. Although it is not shown here, the continuum level of the two models are identical. For the models with  $i < 30^\circ$ , the presence of the disc has little/no effect on the profile shapes. In the figures, the extent of the H $\alpha$  emission is smaller ( $\sim 0.2$  au or  $\sim 20 R_*$ ) compared to the spectro-astrometric observations of Takami et al. (2003) for RU Lup and CS Cha which show 1–5 au scale outflows<sup>1</sup>; however, the extent of the line emission region becomes slightly larger ( $\sim 0.4$  au) if a slower wind acceleration rate ( $\beta = 4$ ) is used.

Although not shown here, we have also computed the H $\alpha$  profiles from the combination of the collimated wind and the accretion disc ( $R_{\text{di}} = 2.2R_*$  and  $R_{\text{do}} = 100$  au) for the same range of  $\beta$  and  $T_{\text{max}}$  values used in Figure 8. As expected (c.f. Figure 11), the models show the decrease in the flux in the blue wing when compared to the flux of the same model computed without the accretion disc. The overall behaviour of the line profile shapes as functions of  $\beta$  and  $T_{\text{wind}}$  are very similar to that for the models without the accretion disc. A significant reduction of the flux in the red wing is seen in the wind model with the accretion disc when compared with the wind only model. The wings appear to be weaker in these models compared to the wind only models because the ratio of the wind emission flux to the continuum flux is lower.

#### 4.4 Magnetosphere + disc + bipolar wind

We examine the characteristics of the line profiles arising from the combination of the magnetospherical accretion flow, the wind, and the accretion disc. For simplicity, the parameters for the magnetosphere ( $T_{\text{max}} = 7500$  K and  $\dot{M}_{\text{acc}} = 10^{-7} \text{M}_\odot \text{yr}^{-1}$  are fixed as in Figure 5), and the wind mass-loss rate, the isothermal wind temperature and the wind anisotropy parameter to  $\dot{M}_{\text{wind}} = 10^{-8} \text{M}_\odot \text{yr}^{-1}$  (i.e.  $\dot{M}_{\text{wind}} = 0.1 \dot{M}_{\text{acc}}$ ),  $T_{\text{wind}}$  and  $b = 4$  respectively. The profile computed for  $i = 55^\circ$  is given in Figure 12, along with the profile computed with the magnetosphere only and

<sup>1</sup> Takami et al. (2003) their observation also show that some objects (e.g Z CMa and AS 353A) displaying the outflows of larger scale ( $> 50$  au); however, this could be formed by shocks rather than MHD-wave heating (e.g. Hartmann et al. 1982) or X-ray heating (e.g. Shang et al. 2002).

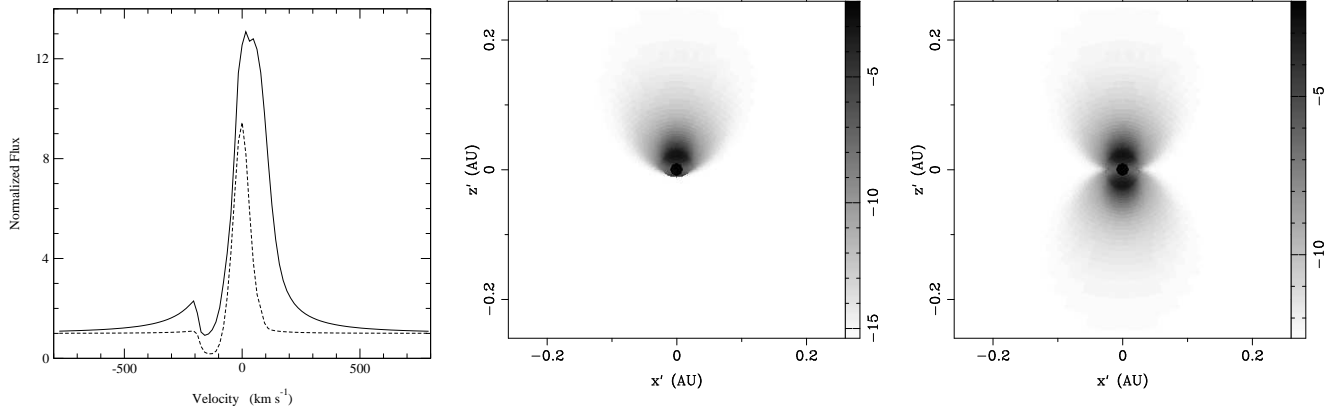


**Figure 11.** A comparison of the wind models with and without the optically-thick and geometrically-thin disc. The latter can be also equivalent to a model with a large inner radius of the accretion disc in which none of the wind emission region is not blocked provided the inclination is moderate. The left panel shows the profile computed with  $i = 55^\circ$ ,  $\beta = 0.5$  and  $T_{\text{wind}} = 9000$  K (see text for other parameters used). The flux in the red wing of the line profile from the model with the disc (solid) is greatly reduced by the presence of the accretion disc compared to that from the model without the disc (dashed). The peak flux and the flux in the wings are also reduced in the model with the disc because the disc does block the wind emission region, but none of the stellar disc, i.e. the continuum flux level is unchanged. The H $\alpha$  image (project in the plane of the observer) for the model with the disc (middle panel) and that for the model without (right plane) are also shown. The image flux is computed by integrating the specific flux over the wavelength range  $-800 \text{ km s}^{-1} < v < 800 \text{ km s}^{-1}$ . The flux is in an arbitrary units and on a logarithmic (base 10) scale.

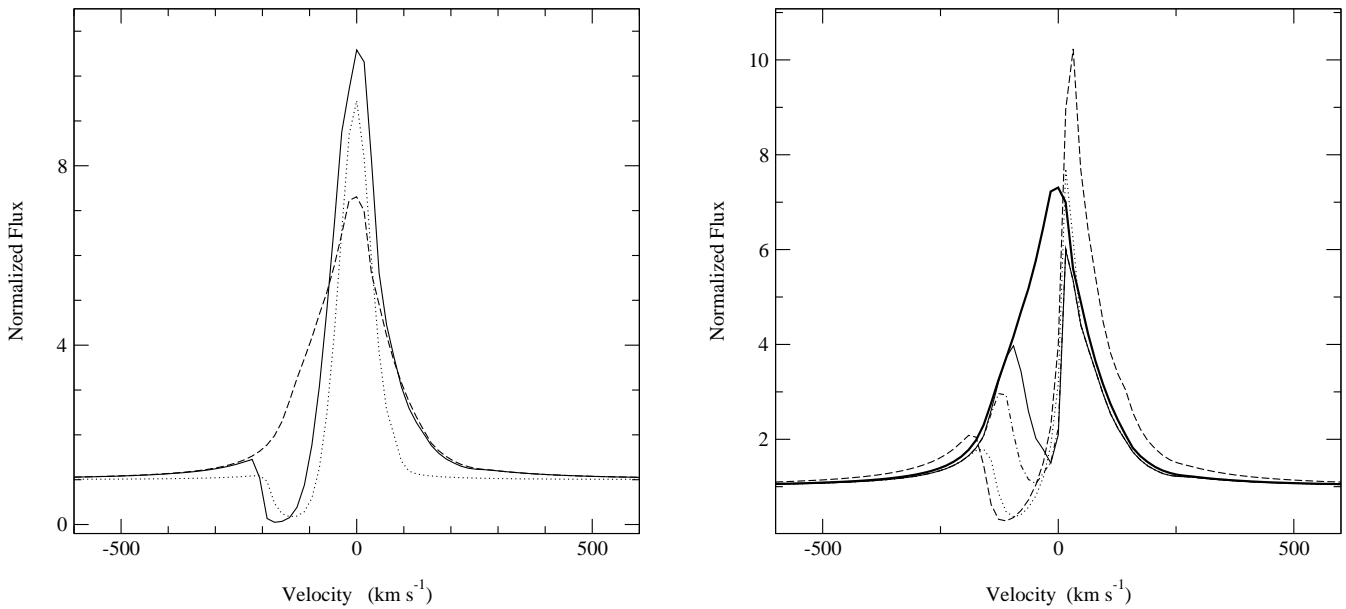


**Figure 12.** A comparison of the profiles computed with the magnetosphere, the wind, the disc, and their combinations. The model configurations used above are: (1) magnetosphere only (dash), (2) wind and disc (dot), and (3) disc, wind and magnetosphere (solid). The parameters used here are  $T_{\text{max}} = 7500$  K,  $\dot{M}_{\text{acc}} = 10^{-7} M_\odot \text{ yr}^{-1}$ ,  $\dot{M}_{\text{wind}} = 10^{-8} M_\odot \text{ yr}^{-1}$ ,  $T_{\text{wind}} = 8000$  K, and  $\beta = 0.5$ . The profile for the case 3 is can be understood as a simple flux sum of the profiles from case 1 and 2.

that with the wind plus accretion disc configurations for a comparison. As one can see from the figure, the profile computed for the disc–wind–magnetosphere hybrid model can be understood as a simple flux sum of the magnetospherical component and the wind component. In this example, the wind causes the absorption of the blue side of the profile, and it adds extra flux around the line centre. As seen before, the presence of the disc causes a reduction in the

**Figure 13.** The effect of the mass-loss rate to mass-accretion rate ratio ( $\mu = \dot{M}_{\text{wind}}/\dot{M}_{\text{acc}}$ ). The H $\alpha$  profile computed with only the magnetospherical accretion (thick solid) —  $T_{\text{max}} = 7500$  K,  $\dot{M}_{\text{acc}} = 10^{-7} M_\odot \text{ yr}^{-1}$  — is compared with the magnetosphere, wind, and disc hybrid models for  $\mu = 0.01$  (solid), 0.025 (dash-dot), 0.1 (dot) and 0.2 (dash). All the models are computed with the inclination angle  $i = 55^\circ$ . As  $\mu$  increases the P-Cygni absorption deepens and the emission component becomes stronger. In general, the absorption is too strong for the models with  $\mu > 0.025$  compared to the observations (e.g., Reipurth et al. 1996).

red side of the profile since the emission from the receding gas is blocked by the disc. The resulting profile appears to be narrower than that of the magnetosphere model.

The effect of changing the ratio of the wind mass-loss rate to mass-accretion rate ( $\mu = \dot{M}_{\text{wind}}/\dot{M}_{\text{acc}}$ ) is demonstrated in

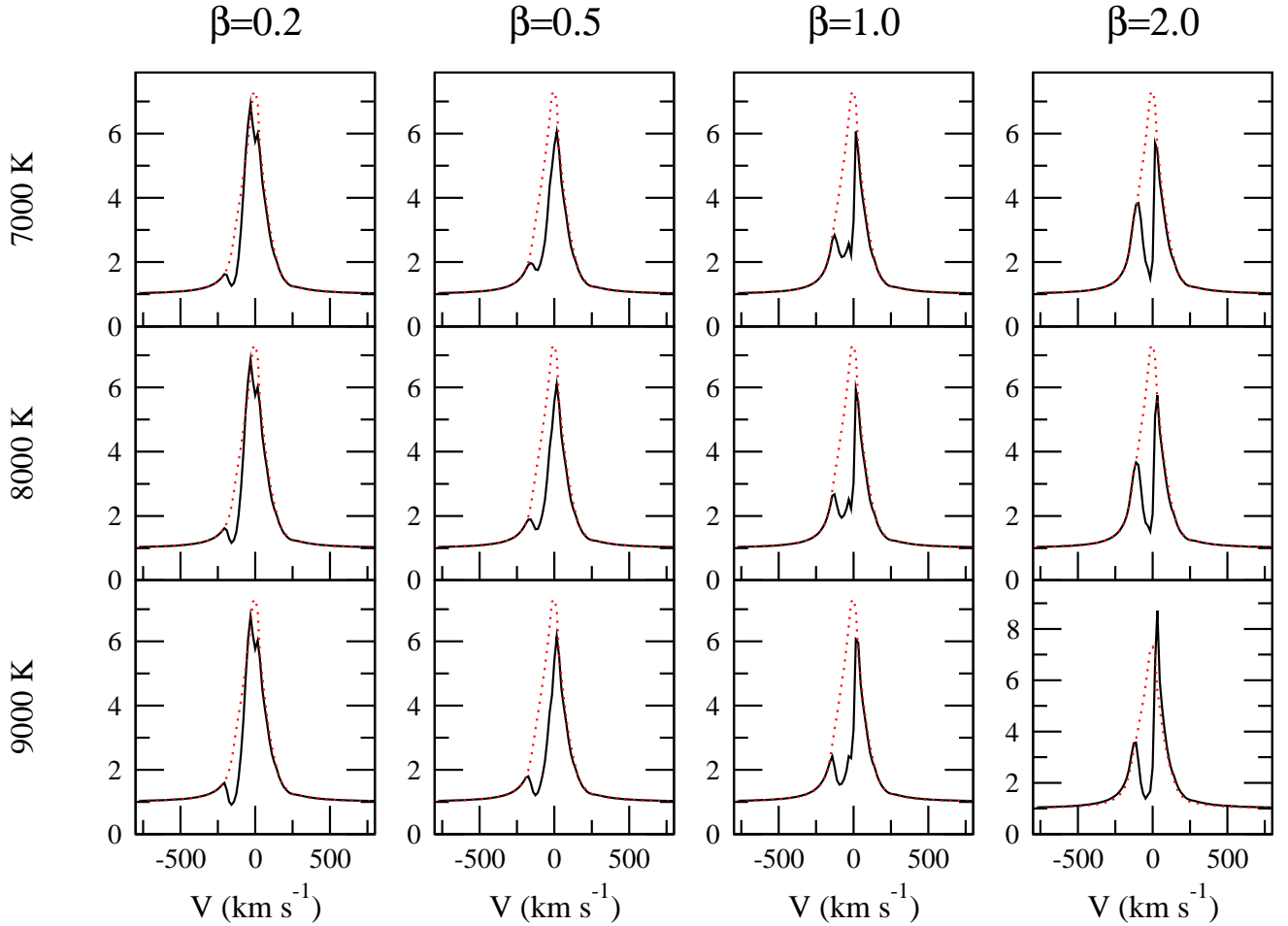


**Figure 14.** Same as Figure 8, but the models include the magnetospherical accretion flow (with  $T_{\max} = 7500$  K and  $\dot{M}_{\text{acc}} = 10^{-7} M_{\odot} \text{ yr}^{-1}$ ), and the accretion disc. The mass-loss rate of the wind is  $\dot{M}_{\text{wind}} = 10^{-9} M_{\odot} \text{ yr}^{-1}$ . A relatively small mass-loss rate is chosen to avoid unrealistically strong P-Cygnus absorption component (see text in section 4.4 and Figure 13). For a comparison, the profile computed with only the magnetospherical accretion flow (dotted) is overlayed. All the profiles are computed at the inclination angle  $i = 55^\circ$ . As  $\beta$  becomes larger, the position of the wind absorption component moves toward the line centre. Although little wind emission is seen in this temperature range, it becomes more important in a model with a higher temperature and a larger wind mass-loss rate. The profiles resemble the observed H $\alpha$  emission profiles affected by the wind.

Figure 13. With a fixed value of mass-accretion rate ( $\dot{M}_{\text{acc}} = 10^{-7} M_{\odot} \text{ yr}^{-1}$ ), the mass-loss rate is varied. The figure shows that as  $\mu$  increases the P-Cygni absorption deepens, and the position of minimum flux in the absorption trough appears to move blue-ward. On the other hand, the emission component becomes stronger as  $\mu$  increases. With this combination of the parameters for the magnetosphere and the wind, the absorption component tends to be too strong for the models  $\mu > 0.025$  (with this model configuration), at all inclinations (not shown here), compared with the observed H $\alpha$  profiles (e.g. Reipurth et al. 1996; Alencar & Basri 2000).

Again, the H $\alpha$  profiles with the same range of the wind temperature ( $T_{\text{wind}}$ ) and the wind acceleration parameter ( $\beta$ ) used in Figure 8 are computed, but this time with  $\mu = 0.01$ . The parameters of the magnetosphere are fixed as in Figure 7. The results are shown in Figure 14 along with the model with only the magnetosphere for a comparison. A relatively small value of  $\mu$  is chosen to avoid absorption component of the P-Cygni profile becoming too strong, as seen in Figure 13. In general, even with small values of the anisotropy parameter ( $b = 0$  and 2), the absorption component is found to be too strong when  $\mu = 0.1$  is used with this combina-

tion of the magnetosphere and the wind. The figure shows that the position of the wind absorption component moves toward the line centre as  $\beta$  becomes larger. Although little wind emission is seen in this temperature range, it becomes more important in a model with a higher temperature and a larger wind mass-loss rate. In fact, the model with  $\beta = 2.0$  and  $T_{\text{wind}} = 9000$  K displays a small amount of the wind emission at  $V \sim 50 \text{ km s}^{-1}$ .

As seen in Figure 12, the profiles shown here can be understood as the combination of the emission from the magnetosphere and the absorption of the flux by the wind component. In general, the emission from the accretion disc is negligible at H $\alpha$  wavelength, but the absorption of the continuum flux from the photosphere by the disc is important for predicting correct line strengths, especially at a high inclination.

Although the profiles shown in Figure 14 are those at a single inclination angle ( $i = 55^\circ$ ), they are very similar to the most common types of H $\alpha$  profiles seen in the observations (e.g. Reipurth et al. 1996). Apparently, this type of profile (affected by the blue-shifted absorption feature) cannot be explained by the magnetospherical accretion flow alone (e.g. Muzerolle et al. 2001). Com-

parison of the model profiles with different types of the observed H $\alpha$  profiles will be given in section 5.1.

#### 4.5 Disc-wind model of Knigge et al. (1995)

As an alternative model for the bipolar wind models (with the combination of the magnetosphere and the accretion disc) shown in Figures 8 and 14, we have also considered the disc-wind model of Knigge et al. (1995) as described in section 4.3. The former resembles the density structure of Krasnopol'sky et al. 2003 in large scale ( $\sim 100$  au) which described in section 2.3.1, and the latter in small scale ( $\sim 10$  au) of the same model. The main difference between the two models are in their density structure. At a given radius, the density increases toward the polar direction in the former model, but the density increases toward the equatorial plane for the models presented here.

First, the disc-wind models without the magnetosphere are considered. Figure 15 shows the H $\alpha$  profiles computed using only the disc-wind component (c.f. Figure 3) for the same isothermal disc-wind temperature ( $T_{\text{dw}}$ ) and the wind acceleration parameter ( $\beta$ ) ranges used for the bipolar wind models. The parameters used for the central star are as in section 2.1, and the other disc-wind parameters are summarised in Table 3. The figure shows that the wind emission increases as  $\beta$  and  $T_{\text{dw}}$  increase. Similar to the bipolar wind models, the location of the P-Cyg absorption component moves toward the line centre as  $\beta$  increases. The morphology of the profile exhibited by the model changes from FU-Ori type for the models with small  $\beta$  to the stronger emission types which are more commonly seen in the observed H $\alpha$  (c.f. Reipurth et al. 1996) as the value of  $\beta$  increases. Although not shown here, we find that the profile shapes are relatively insensitive to the value of the wind collimation parameter  $d$ . The dependency on the disc wind mass-loss rate of the profile shape is similar to that of the collimated wind models (Figure 13).

We now consider the models computed with the combination of the disc-wind and the magnetospherical accretion components. The parameters used for the magnetosphere are set to be same as in the case for Figure 7, and are kept constant for simplicity. The mass-loss rate of the disc wind is set to  $\dot{M}_{\text{dw}} = 10^{-8} M_{\odot} \text{ yr}^{-1}$  (i.e.  $\mu = \dot{M}_{\text{dw}}/\dot{M}_{\text{acc}} = 0.1$ ). Figure 16 shows the models profiles computed using the same ranges of the disc-wind temperature and the wind acceleration parameter as in the previous cases.

As in the disc wind only models (Figure 15), the location of the absorption component moves toward the line centre as the value of  $\beta$  increases (the wind acceleration is slower). The figure shows that in the models with smaller  $\beta$  and  $T_{\text{dw}}$ , the line emission from the magnetosphere dominates. On the other hand, in the models with larger  $\beta$  and  $T_{\text{dw}}$ , the emission from the disc wind dominates. Compared to the observation of Reipurth et al. (1996) and Alencar & Basri (2000), the lines are too strong for ( $T_{\text{dw}}, \beta$ ) = (9000 K, 2.0) and (9000 K, 1.0) models.

Although the models in Figure 16 are computed with limited ranges of  $T_{\text{dw}}$  and  $\beta$ , the resulting profiles exhibit the wide varieties of line shapes which are very similar to the types of H $\alpha$  profiles seen in the observations (c.f. Reipurth et al. 1996). The shape of the primary and secondary peaks in the profiles are slightly “rounder” compared to those of the accretion, collimated wind, disc hybrid model shown in Figure 14. The rounder peaks are caused by the rotation of the wind. The profiles from the disc-wind models are affected more by the rotational motion of the wind since the gas is more concentrated toward the equator, but in the models with the

**Table 3.** A summary of the standard disc-wind model parameters used in section 4.5. See also section 2.3.2.

$d$ [ $R_*$ ]	$R_{\text{wi}}$ [ $R_*$ ]	$R_{\text{wo}}$ [au]	$\dot{M}_{\text{dw}}$ [ $M_{\odot} \text{ yr}^{-1}$ ]	$p$ [-]	$f$ [-]	$R_s$ [ $R_*$ ]
21.4	3.0	1.0	$10^{-8}$	-3/2	2.0	30

collimated wind the gas is concentrated more in the polar directions.

We note the ambiguity seen between some of the disc-wind only models and the disc-wind, magnetosphere hybrid models. For example, the disc-wind only model with  $(T_{\text{wind}}, \beta) = (8000 \text{ K}, 1.0)$  in Figure 15 and the disc-wind model with  $(T_{\text{wind}}, \beta) = (9000 \text{ K}, 0.5)$  in Figure 16 give very similar profiles. Given such an observed profile, it is difficult to distinguish if the emission is dominated by the accretion or the wind unless some other lines, not affected associated with wind or magnetosphere, are used simultaneously.

General characteristics of the profiles from the disc-wind, magnetosphere hybrid model (Figure 16) are very similar to those of the disc, collimated wind, magnetosphere hybrid model (Figure 14). The main difference between these two sets of models is in the ration of the mass-loss rate to the mass accretion rate,  $\mu$ . While the models presented in this section use  $\mu = 0.1$  which is consistent with the MHD jet models (e.g. Königl & Pudritz 2000), the models in Figure 14 use much smaller value ( $\mu = 0.01$ ). The dependency of the model profiles on the inclination angle for the two different wind models will be discussed in the next section.

## 5 DISCUSSION

### 5.1 Classification scheme proposed by Reipurth et. al (1996)

Reipurth et al. (1996) proposed the two-dimensional classification of H $\alpha$  emission profiles of T Tauri stars and Herbig Ae/Be stars. Their classification scheme contains four classes (I, II, III and IV) differentiated by the ratio of the secondary-to-primary emission components in the profiles. Each classes are divided into two subclasses (B and R) which depends whether the absorption component is on the blue or red side. Readers are referred to Fig. 4 of their paper. Figure 17 shows the sample model profiles which are classified according to the definition of Reipurth et al. (1996). The combination of the disc wind, magnetospherical accretion, and accretion disc can reasonably reproduce all the classes of the profiles seen in observations. Similar profiles can be reproduced if the bipolar wind is used instead of the disc wind, but the wind absorption at a given velocity location occurs at a different inclination angles when the wind type is switched from the bipolar wind to the disc wind. The corresponding parameters (of the disc-wind, magnetosphere, hybrid model) used to reproduce the profiles in the figure are given in Table 4 along with brief comments on possible physical conditions which leads to the profiles in each class. In the following, we will discuss each classification type of Reipurth et al. (1996) based on our model results.

**Type I:** Using the samples of H $\alpha$  from 43 CTTS, Reipurth et al. (1996) found this type to be the second most common (26 per cent) among them. Type I (symmetric around line centres), is mainly produced in the magnetosphere. Although not shown here, this type of profile can be also reproduced with the disc-

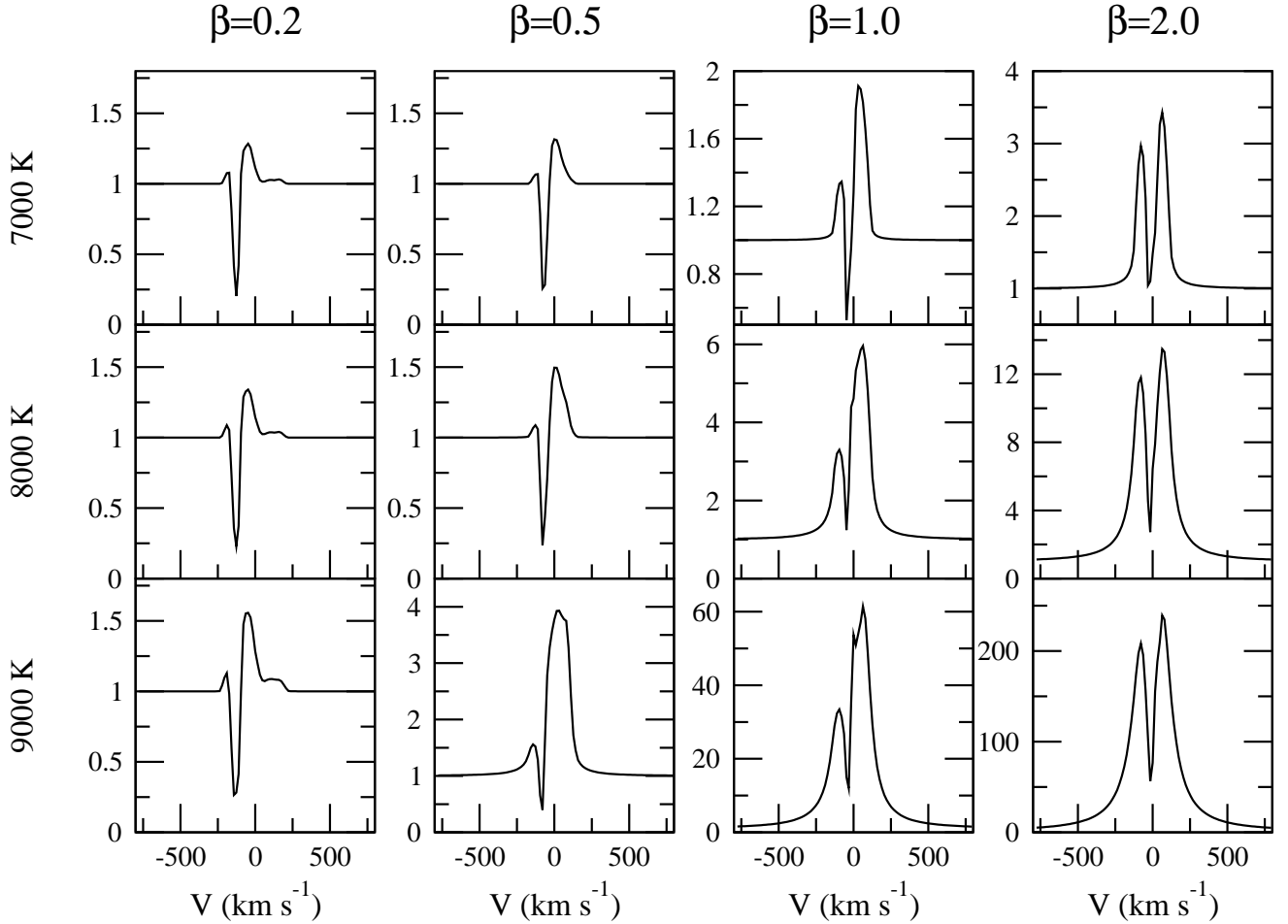


**Figure 15.** The H $\alpha$  profiles computed with the disc-wind only models. With the wind mass-loss rate fixed at  $\dot{M}_{\text{dw}} = 10^{-8} \text{ M}_\odot \text{ yr}^{-1}$ , the line profiles are computed with different combinations of the wind acceleration rate ( $\beta$ ) and the isothermal disc-wind temperature ( $T_{\text{dw}}$ ). The wind emission increases as the values of  $\beta$  and  $T_{\text{wind}}$  increase (as the wind becomes accelerates slower and as the wind comes warmer). As in the bipolar wind models (Figure 8), the position of the wind absorption moves toward the line centre as  $\beta$  becomes larger. The morphology of the profiles are similar to that of observations.

wind, magnetosphere hybrid model with low inclination angles ( $<\sim 10^\circ$ ). Since there is no material in the polar region in the disc wind model, the observer can look the magnetosphere almost directly for high inclination cases, provided that wind temperature is low enough so that the wind emission is negligible. The bipolar wind, magnetosphere and accretion hybrid model with high inclination ( $70^\circ - 80^\circ$ ) can also give this type of profile since the influence of the bipolar wind is minimum in the equatorial directions. The wind acceleration parameter for the bipolar wind must be relatively small ( $\beta <\sim 0.5$ ).

**Type II-B:** This type can be produced by the disc-wind magnetosphere hybrid models at moderate to high inclination angles with wide ranges of the wind acceleration rate ( $\sim 0.2 < \beta < \sim 2.0$ ) and the wind temperature ( $\sim 7000 \text{ K} < T < \sim 9000 \text{ K}$ ). If the inclination is high ( $i \sim 80^\circ$ ), the disc-wind acceleration parameter should be relatively small ( $\beta < \sim 0.5$ ). If the inclination is moderate ( $i \sim 60^\circ$ ), the wind acceleration parameter should be relatively high ( $\beta > \sim 2.0$ ). This type can be also produced in the bipolar wind, magnetosphere disc hybrid model with similar ranges of inclinations ( $\sim 60^\circ < i < \sim 80^\circ$ ) and temperatures ( $\sim 7000 \text{ K} < T < \sim 9000 \text{ K}$ ), but the wind acceleration should be always high ( $\beta > \sim 1.0$ ).

**Type II-R:** The physical conditions which result in this type is very similar to those of Type II-B according to the disc-wind magnetosphere hybrid models. The main difference is between the two is in their inclination angles. This type is more likely seen at higher inclination angles ( $i \sim 80^\circ$ ) compared to Type II-B. With the bipolar wind model, the wind acceleration parameter must be very large ( $\beta \sim 6.0$ ) to produce this type, and the inclination must be moderate to low ( $i < \sim 60^\circ$ ). This type is rarely seen in the bipolar wind models with the nominal parameter ranges i.e.  $\sim 0.2 < \beta < \sim 2.0$  and  $\sim 7000 \text{ K} < T < \sim 9000 \text{ K}$ . More common in the models with the disc wind.

**Type III-B:** This type is the most commonly seen profiles in the CTTS H $\alpha$  samples in Reipurth et al. (1996). Interestingly, the most common profile type seen in both the bipolar wind, disc, magnetosphere hybrid models and the disc-wind, magnetosphere hybrid model are Type III-B profiles (c.f. Figures 14 and 16). In this type of profiles, the main emission comes from the magnetosphere, and the profile shape is altered from a slightly blue-asymmetric one to a slightly red-asymmetric one via the wind absorption in the blue wing. In the models with the disc-wind, the acceleration parameter should be relatively small ( $\beta < 0.5$ ). The profile type changes from Type III-R to Type II-R if the value of  $\beta$  increases. The inclination

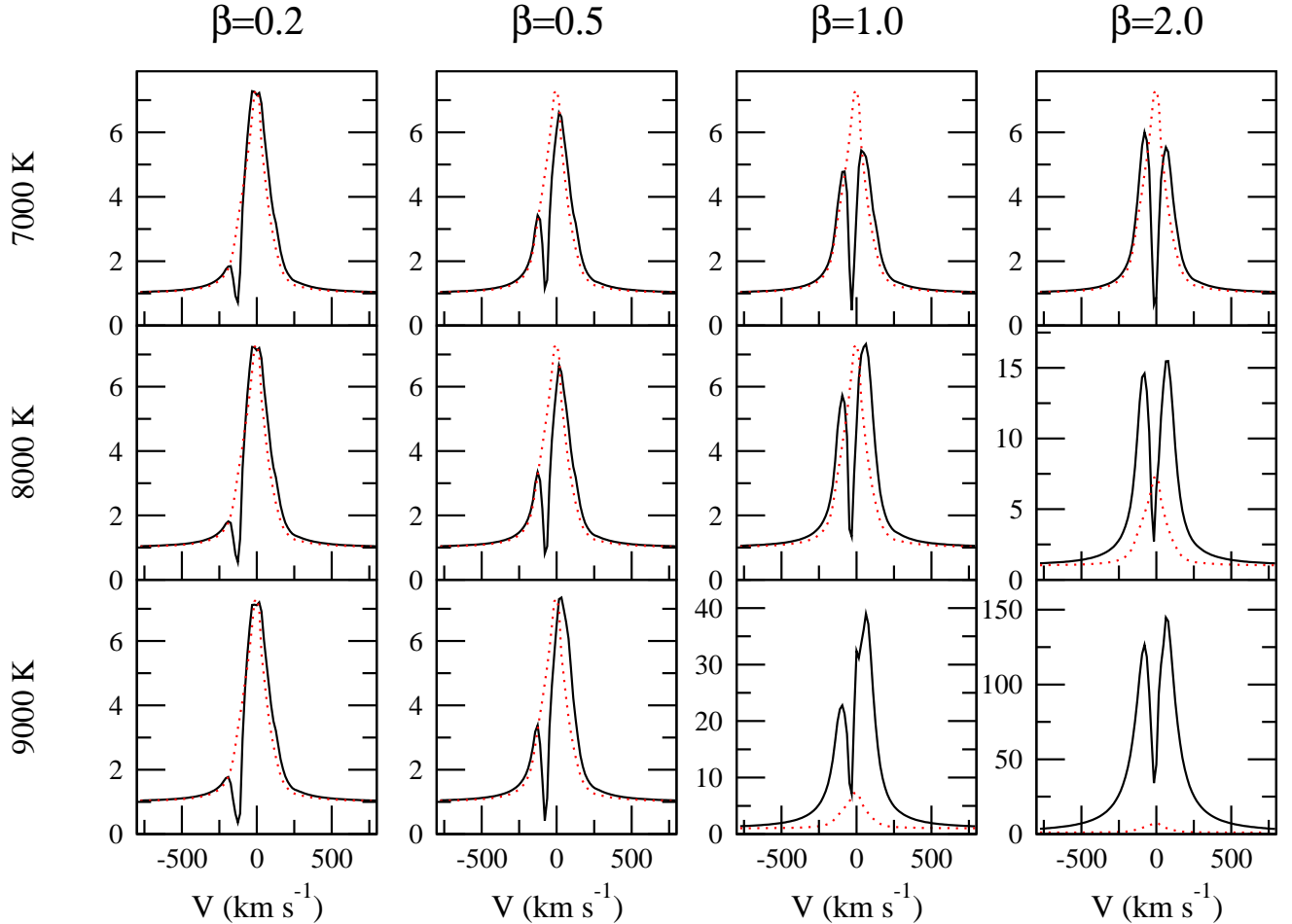


**Figure 16.** The disc-wind, magnetosphere hybrid model. The same as Figure 15, but these models (solid) also include the magnetosphere accretion flow ( $T_{\max} = 7500$  K and  $\dot{M}_{\text{acc}} = 10^{-8} M_{\odot} \text{ yr}^{-1}$ ). While the emission from the magnetosphere dominates for the models with smaller  $\beta$  and  $T_{\text{dw}}$  (the faster acceleration and the colder wind models), the emission from the wind dominates the profiles for models with larger  $\beta$  and  $T_{\text{dw}}$  (the slower acceleration and the hotter models). For a comparison, the profile computed with only the magnetospherical accretion flow (dotted) is overlayed.

angles must be moderate to high ( $\sim 60^\circ < i < \sim 80^\circ$ ). On the other hand, the inclination must be low to moderate ( $i < \sim 60^\circ$ ) in the models with the bipolar wind. The difference in the inclination dependency occurs since the density distribution of the two types of the winds are different.

**Type III-R:** This is the least common type of the observed profile (2 per cent) according to Reipurth et al. (1996). Incidentally, we also found it difficult to reproduce this type of profile since this can be achieved only at narrow range of parameter space (very high inclination angle with a disc wind model,  $T_{\max} \sim 8300$  K, and  $\dot{M}_{\text{acc}} \sim 10^{-8} M_{\odot} \text{ yr}^{-1}$ ). Similarly, in the models with the bipolar wind, the inclination angle must be very high (close to edge on) to produce this type of profile. Since the inclination angles must be high for both wind models, this indicates that the accretion disc plays an important role in producing this type of the profile, but not the wind. The rareness of this type in the observation can be understood by the required high inclination angle (almost edge-on) in our models.

**Type IV-B:** This type of the profiles is very similar to Type III-B, but the wind in this type of profile may be accelerating faster (a smaller  $\beta$  value) than that in Type III-B. In the models with the disc-wind, this type is seen at moderate to high inclinations

( $\sim 60^\circ < i \sim 80^\circ$ ) with relatively small value of the acceleration parameters ( $\beta < \sim 0.5$ ). In the models with the bipolar wind, this type is commonly seen at moderate to low inclinations ( $i \sim < 60^\circ$ ). The difference in the inclination dependency occurs because of the density distribution of the two types of the winds are different.

**Type IV-R:** This is the second least common type of observed profile (5 per cent) which shows the inverse P-Cyg profile shape. This can be understood since the magnetospherical accretion model of Hartmann et al. (1994) predicts that the redshifted absorption can occur at a limited range of inclination angle ( $i = \sim 50^\circ$ , but depends on the geometry of the magnetosphere) with which the hot continuum flux from the footprint of the magnetosphere is seen through relatively fast moving gas in the accretion stream. The wind component must be very weak. The mass-accretion rate should be much lower ( $\dot{M}_{\text{acc}} \sim 10^{-9} M_{\odot} \text{ yr}^{-1}$ ) than that of the models which produce Type I profiles since the flux in the broadening wings can not be too high to produce the inverse P-Cyg profile.

**Table 4.** The summary model parameters for the profiles in Figure 17 and brief comments. The temperatures are in  $10^3$  K.  $\dot{M}_{\text{acc}}$  and  $\dot{M}_{\text{dw}}$  are in  $M_{\odot} \text{ yr}^{-1}$ .

Class	$i$	$\dot{M}_{\text{acc}}$	$T_{\text{max}}$	$\dot{M}_{\text{dw}}$	$T_{\text{dw}}$	$\beta$	Comment
I	55	$10^{-7}$	7.5	—	—	—	Accretion dominated possibly without the wind. Mid inclination.
II-B	55	$10^{-7}$	7.5	$10^{-8}$	8.0	1.0	Wind, disc and magnetosphere. Wide range of wind acceleration rate. Mid–high inclination
III-B	55	$10^{-7}$	7.5	$10^{-8}$	9.0	0.5	Wind, disc and magnetosphere. Fast–mid wind acceleration rate. Mid–high inclination
IV-B	55	$10^{-7}$	7.5	$10^{-8}$	9.0	0.2	Wind, disc and magnetosphere. Fast wind acceleration rate. Mid–high inclination
II-R	80	$10^{-7}$	7.5	$10^{-8}$	7.0	2.0	Wind, disc and magnetosphere. Slow wind acceleration rate. High inclination
III-R	85	$10^{-8}$	8.2	$10^{-9}$	6.0	1.0	Wind, disc and magnetosphere. Mid wind acceleration rate. Very high inclination
IV-R	55	$10^{-9}$	9.5	—	—	—	Accretion dominated. Low mass-accretion rate. Mid inclination.

## 5.2 Which wind model?

In the previous sections, two possible geometrical configurations for the wind from CTTS were considered: (1) a bipolar wind, and (2) a disc wind. While the material is more concentrated toward the polar regions for a given radius in the first case, the material is more concentrated toward the equatorial plane in the second case.

The distinct difference in the density dependency on the polar angles in two models should be apparent in the inclination angle dependency on the shapes of the line profiles. Figure 18 shows the H $\alpha$  profiles computed for 1. the disc, bipolar-wind, accretion hybrid model (section 4.4) and 2. the disc-wind, magnetosphere hybrid model (section 4.5) at inclination angles  $i = 10^\circ, 55^\circ$  and  $80^\circ$ . Both models include the magnetospherical accretion component with the same parameters used as in sections 4.4 and 4.5 i.e.  $T_{\text{max}} = 7500$  K and  $\dot{M}_{\text{acc}} = 1 \times 10^{-7} M_{\odot} \text{ yr}^{-1}$ .

Mainly because of the geometrical configuration, the P-Cyg absorption feature weakens as the inclination increases for the model with the bipolar wind. The optical depth to an observer is higher (from the wind emission region) for with a lower inclination angle with this geometry. Although not shown here, this tendency of the inclination dependency holds for the models with bipolar wind models for wide ranges of  $\beta$  and  $T_{\text{wind}}$ . For the model with the disc wind, the absorption becomes stronger as the inclination becomes larger. The optical depth to an observer becomes larger as the inclination increases in this geometry.

Similarly, the line equivalent width increases as the inclination angle increases for the model with the bipolar wind, it decreases as the inclination angle increases for the model with the disc wind. For the models with only magnetosphere (section 4.1), we find that the line equivalent width decreases as the inclination increases in those models (see Figure 7). Interestingly, the observational study of Appenzeller et al. (2005) showed that the H $\alpha$  line equivalent width of CTTS increases as the inclination angle increases. Only the models with the bipolar wind agree with the trend seen in their observation. Although the uncertainty in the inclination angles of the observed object might be large, a larger sample in addition to that of Appenzeller et al. (2005) for further investigation of the inclination dependency on the line profile will be extremely useful for determining the wind configuration of CTTS.

Despite the inclination angle dependency of the observed H $\alpha$  favouring the models with bipolar wind, there are two main aspects of this model which are not quite consistent with the magneto-centrifugal launched jet numerical models (e.g. Krasnopolsky et al. 2003). First, in section 4.4, we found that the ratio of the mass-loss to mass-accretion rates needed to be rather small ( $\mu < \sim 0.025$ ), in order not to have an unrealistically strong P-Cyg absorption component, compared to the MHD simulations suggested (Königl &

Pudritz 2000) i.e.  $\mu \approx 0.1$ . Considering large uncertainty in MHD theories and observational measurements (e.g.  $\dot{M}_{\text{acc}}$ ,  $\dot{M}_{\text{wind}}$  and  $B$ ), the wide range of the mass-loss to mass-accretion ratio may be still reasonable. On the other hand, the models with the disc wind (section 4.5) using  $\mu = 0.1$  reproduces the profiles (Figure 16) similar to that seen in observations. Second, the MHD models predict that the wind/jet becomes collimated well above the disc plane ( $> 10$  au), but our bipolar wind model are collimated (density enhanced toward in the polar direction) from right outside of the magnetosphere. Unless the origin of the wind is from the central star itself, the density distribution used for the bipolar wind is not quite consistent with the near field of the MHD jet models, considering that the most of the H $\alpha$  emission occurs within a few to a several radii of the magnetosphere (Figure 11). The density structure used for the disc wind model, however, is very similar to that of MHD simulations in the near field where the most of the H $\alpha$  wind emission occurs. Interestingly, however, the recent study of Matt & Pudritz (2005) demonstrated the possibility that the stellar wind along the open magnetic field originated from the star can cause significant spin-down torque on the star, provided that mass-loss rate is high enough. Considering the issues mentioned above, it is not possible to favour the bipolar wind model to the disc wind model without further observational constraints. In reality, two types of the winds (bipolar wind and disc wind) may co-exists similar to that seen in e.g. Drew, Proga, & Stone (1998) and Matt & Pudritz (2005). In these models, the fast stellar wind is present in the polar directions, and at the same time the slower disc wind is present near the equatorial plane.

One possible way to distinguish the two different wind models is to examine the profile shape of a CTTS which is known to be viewed at pole-on. If the profile contains a prominent blue-shifted absorption component (e.g. Type IV-B), the system is more likely to be associated with the bipolar wind type of outflow (but not with the disc-wind type of outflow).

## 6 CONCLUSIONS

We have presented the disc–wind–magnetosphere hybrid radiative transfer models for classical T Tauri stars, and detailed studies of the H $\alpha$  formation from their complex to circumstellar environment to understand the wide variety of H $\alpha$  profiles seen in observations. The two types of wind models considered are (1) the bipolar wind model in which the wind originates from the star itself (section 2.3.1; Figure 1), and (2) the disc-wind model in which the wind originates from the inner part of the accretion disc (section 2.3.2; Figure 3). We found that both wind models combined with the mag-

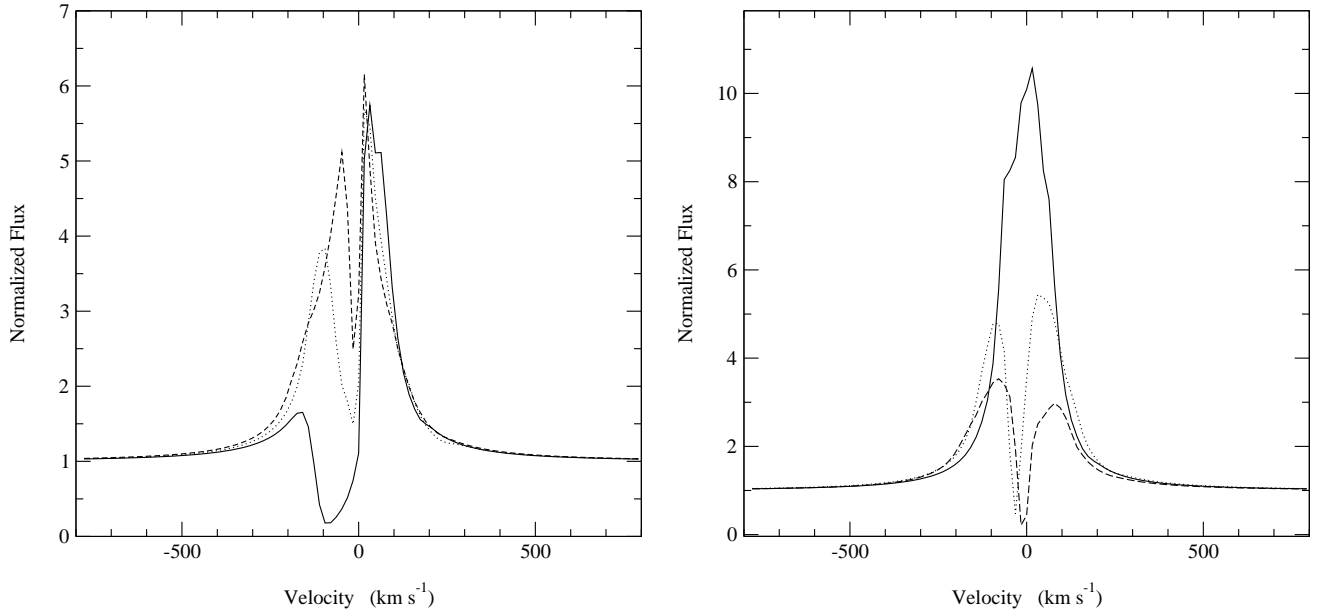


**Figure 18.** Dependency of the  $H\alpha$  model profiles on the inclination angle. The profiles computed at  $i = 10^\circ$  (solid),  $55^\circ$  (dot) and  $80^\circ$  (dash) using 1. the disc, bipolar-wind, accretion hybrid model (left panel; c.f. section 4.4) and 2. using the disc-wind, magnetosphere hybrid model (right; c.f. section 4.5) are shown for a comparison. The parameters used for the magnetosphere are same for the both models, i.e.  $T_{\max} = 7500$  K and  $\dot{M}_{\text{acc}} = 10^{-7} M_\odot \text{ yr}^{-1}$ . The isothermal wind temperature and the wind acceleration parameter used in both models are  $T = 7000$  K and  $\beta = 1.0$  respectively. All the other parameters are same as in sections 4.4 and 4.5. While the line equivalent width increases as the inclination angle increases for the former model configuration, it decreases as the inclination angle increases for the latter. Only the former agrees with the tendency seen in the observational study of Appenzeller et al. (2005) who showed that the  $H\alpha$  line equivalent width of CTTS increases as the inclination angle increases.

netospherical accretion flow reproduces the wide variety of  $H\alpha$  profiles (Figures 14 and 16) seen in the observations.

The inclination dependency of the line equivalent width predicted by the bipolar wind model agree with trends seen in the observation, but the disc-wind model does not. With the standard magnetospherical configuration (Table 1), the ratio of the mass-loss to mass-accretion rates ( $\mu$ ) used in the bipolar wind was set to be 4–10 times smaller than that predicated by magneto-hydrodynamical (MHD) calculations (c.f.  $\mu \sim 0.1$ ; Königl & Pudritz 2000) to avoid the blue-shifted absorption component becoming unrealistically too strong; however  $\mu$  used in the disc-wind models are consistent with MHD calculations.

Using the model results, we examined the  $H\alpha$  spectroscopic classification proposed by Reipurth et al. (1996), and discussed the basic physical conditions that reproduce the profiles in each classified type. Using the different combinations of the inclination ( $i$ ), the mass-loss to mass-accretion rate ratio ( $\mu$ ) and the wind acceleration rate ( $\beta$ ), our radiative transfer model was able to produce all 7 types of the profiles in Reipurth et al. (1996).

Similar model configurations used here may be also applicable to Herbig Ae/Be and brown dwarfs since their  $H\alpha$  observations also exhibit evidence of the outflow and inflow (e.g. Finkenzeller & Mundt (1984); Muñoz et al. 2005), but no model has been developed to explain the phenomenon. Further investigation on the possibility of applying our model to these objects are needed.

Future work should include the followings: (1) Improving the wind models. The parametrisation of the wind density structure should be changed to follow more closely that of MHD simulations. The wind temperature structure should be calculated self-consistently (c.f. Hartmann et al. 1994; Martin 1996). (2) Computing the line profiles using the density structure from MHD directly.

Check the consistency, and give feedback to the MHD models which are needed to be tested against observational data. (3) Spectropolarimetric study to explore the geometry and the rotation of the disc (e.g. Vink et al. 2005). (4) Modelling of the extended  $H\alpha$  and spectro-astrometric observations (c.f. Takami et al. 2003; Appenzeller et al. 2005). (5) Line variability study using a 3D radiative transfer model (e.g. Symington et al. 2005a; Kurosawa et al. 2005) to probe the geometrical structure.

## ACKNOWLEDGEMENTS

Authors thank Jorick Vink for providing us the  $H\alpha$  data of T Tau. This work is supported by PPARC standard grant PPA/G/S/2001/00081.

## References

- Alencar S. H. P., Basri G., 2000, AJ, 119, 1881
- Alencar S. H. P., Basri G., Hartmann L., Calvet N., 2005, A&A, 440, 595
- Anders E., Grevesse N., 1989, geochim. cosmochim. acta, 53, 197
- Appenzeller I., Bertout C., Stahl O., 2005, A&A, 434, 1005
- Appenzeller I., Mundt R., 1989, A&AR, 1, 291
- Basri G., Bertout C., 1989, ApJ, 341, 340
- Bertout C., Basri G., Bouvier J., 1988, ApJ, 330, 350
- Blandford R. D., Payne D. G., 1982, MNRAS, 199, 883
- Burrows C. J., Stapelfeldt K. R., Watson A. M., Krist J. E., Ballester G. E., Clarke J. T., Crisp D., Gallagher J. S., Griffiths R. E., Hester J. J., Hoessel J. G., Holtzman J. A., Mould J. R., Scowen P. A., Trauger J. T., Westphal J. A., 1996, ApJ, 473, 437

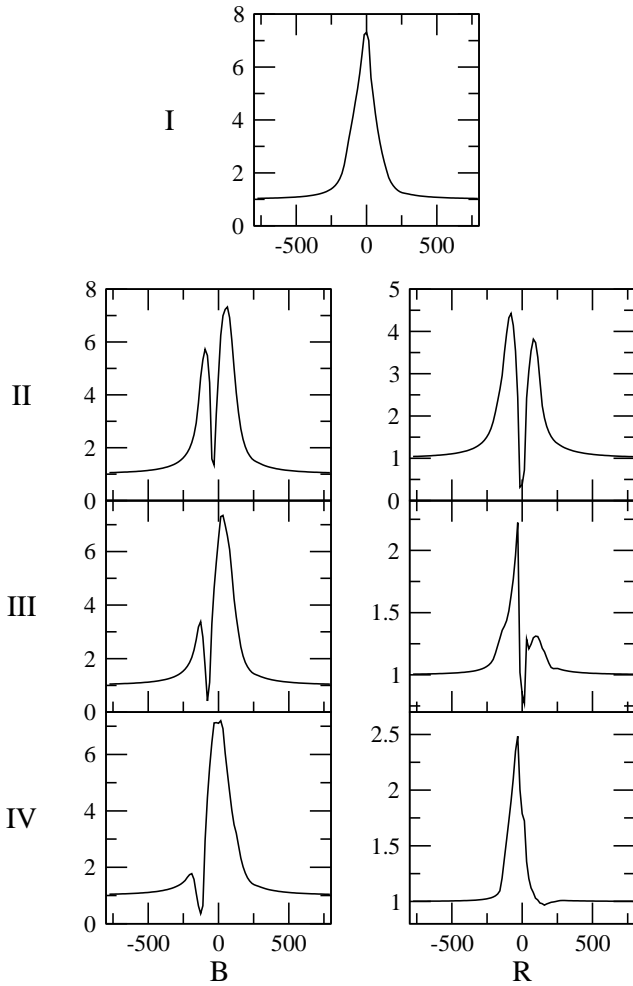


**Figure 17.** Sample H $\alpha$  model profiles which characterise the classification by Reipurth et al. (1996). The combination of magnetospheric accretion flow, the accretion disc, and the disc wind model can reasonably reproduce wide ranges of H $\alpha$  profiles seen in observations. Similar results can be obtained if the bipolar wind is replaced by the disc wind. The model parameters and short comments are summarised in Table 4. The horizontal axes are velocities in km s $^{-1}$ , and the vertical axes are normalised flux.

- Calvet N., Basri G., Kuhi L. V., 1984, ApJ, 277, 725  
 Calvet N., Hartmann L., Hewett R., 1992, ApJ, 386, 229  
 Camenzind M., 1990, Reviews of Modern Astronomy, 3, 234  
 Castor J. I., Abbott D. C., Klein R. I., 1975, ApJ, 195, 157  
 Castor J. I., Lamers H. J. G. L. M., 1979, ApJS, 39, 481  
 Chiang E. I., Goldreich P., 1997, ApJ, 490, 368  
 Collier Cameron A., Campbell C. G., 1993, A&A, 274, 309  
 Cotera A. S., Whitney B. A., Young E., Wolff M. J., Wood K., Povich M., Schneider G., Rieke M., Thompson R., 2001, ApJ, 556, 958  
 Decampi W. M., 1981, ApJ, 244, 124  
 Draine B. T., Lee H. M., 1984, ApJ, 285, 89  
 Drew J. E., Proga D., Stone J. M., 1998, MNRAS, 296, L6  
 Edwards S., Cabrit S., Strom S. E., Heyer I., Strom K. M., Anderson E., 1987, ApJ, 321, 473  
 Edwards S., Hartigan P., Ghandour L., Andrulis C., 1994, AJ, 108, 1056  
 Finkenzeller U., Mundt R., 1984, A&AS, 55, 109  
 Frank J., King A., Raine D. J., 2002, Accretion Power in Astro-

- physics, 3rd edn. Cambridge Univ. Press, Cambridge, p. 398  
 Ghosh P., Pethick C. J., Lamb F. K., 1977, ApJ, 217, 578  
 Grevesse N., Noels A., 1993, in Origin and Evolution of the Elements, N. P., E. V.-F., M. C., eds., Cambridge Univ. Press, Cambridge, p. 15  
 Guenther E. W., Emerson J. P., 1996, A&A, 309, 777  
 Gullbring E., Hartmann L., Briceno C., Calvet N., 1998, ApJ, 492, 323  
 Hanner M., 1988, in NASA Conf. Pub. 3004, 22, Vol. 3004, p. 22  
 Harries T. J., 2000, MNRAS, 315, 722  
 Hartigan P., Edwards S., Ghandour L., 1995, ApJ, 452, 736  
 Hartmann L., Avrett E., Edwards S., 1982, ApJ, 261, 279  
 Hartmann L., Hewett R., Calvet N., 1994, ApJ, 426, 669  
 Herbig G. H., 1962, Advances in Astronomy and Astrophysics, 1, 47  
 Hillier D. J., 1991, A&A, 247, 455  
 Johns-Krull C. M., Valenti J. A., Hatzes A. P., Kanaan A., 1999, ApJ, 510, L41  
 Kenyon S. J., Hartmann L., 1987, ApJ, 323, 714  
 Kenyon S. J., Hartmann L., Hewett R., Carrasco Cruz-Gonzalez I., Recillas E., Salas L., Serrano A., Strom K. M., Strom S. E., Newton G., 1994, AJ, 107, 2153  
 Kim S., Martin P. G., Hendry P. D., 1994, ApJ, 422, 164  
 Klein R. I., Castor J. I., 1978, ApJ, 220, 902  
 Knigge C., Woods J. A., Drew E., 1995, MNRAS, 273, 225  
 Königl A., 1991, ApJ, 370, L39  
 Königl A., Pudritz R. E., 2000, Protostars and Planets IV, 759  
 Krasnopolsky R., Li Z.-Y., Blandford R. D., 2003, ApJ, 595, 631  
 Kuhi L. V., 1964, ApJ, 140, 1409  
 Kurosawa R., Harries T. J., Bate M. R., Symington N. H., 2004, MNRAS, 351, 1134  
 Kurosawa R., Harries T. J., Symington N. H., 2005, MNRAS, 358, 671  
 Kurosawa R., Hillier D. J., 2001, A&A, 379, 336  
 Kurucz R. L., 1979, ApJS, 40, 1  
 —, 1993, VizieR Online Data Catalog, 6039, 0  
 Kwan J., Tademaru E., 1995, ApJ, 454, 382  
 Long K. S., Knigge C., 2002, ApJ, 579, 725  
 Luttermoser D. G., Johnson H. R., 1992, ApJ, 388, 579  
 Malbet F., Benisty M., De Wit W. J., Kraus S., Meilland A., Millour F., Tatulli E., Berger J., Chesneau O., Hofmann K., Isella A., Natta A., Petrov R., Preibisch T., Stee P., Testi L., Weigelt G., AMBER Collaboration, 2005, ArXiv Astrophysics e-prints  
 Martin S. C., 1996, ApJ, 470, 537  
 Mathis J. S., Rumpl W., Nordsieck K. H., 1977, ApJ, 217, 425  
 Matt S., Pudritz R. E., 2005, ApJ, 632, L135  
 Mihalas D., 1978, Stellar atmospheres, 2nd edn. W. H. Freeman and Co., San Francisco  
 Muzerolle J., Calvet N., Hartmann L., 2001, ApJ, 550, 944  
 Muzerolle J., Luhman K. L., Briceño C., Hartmann L., Calvet N., 2005, ApJ, 625, 906  
 Ouyed R., Pudritz R. E., 1997, ApJ, 482, 712  
 Pudritz R. E., Banerjee R., 2005, in IAU Symposium, pp. 163–173  
 Ray T. P., Mundt R., Dyson J. E., Falle S. A. E. G., Raga A. C., 1996, ApJ, 468, L103  
 Reipurth B., Pedrosa A., Lago M. T. V. T., 1996, A&AS, 120, 229  
 Rybicki G. B., Hummer D. G., 1978, ApJ, 219, 654  
 Shakura N. I., Sunyaev R. A., 1973, A&A, 24, 337  
 Shang H., Glassgold A. E., Shu F. H., Lizano S., 2002, ApJ, 564, 853  
 Shu F. H., Najita J., Ostriker E., Wilkin F., Ruden S., Lizano S., 1994, ApJ, 429, 781

- Steinacker J., Henning T., Bacmann A., Semenov D., 2003, *A&A*, 401, 405
- Symington N. H., Harries T. J., Kurosawa R., 2005a, *MNRAS*, 356, 1489
- Symington N. H., Harries T. J., Kurosawa R., Naylor T., 2005b, *MNRAS*, 358, 977
- Takami M., Bailey J., Chrysostomou A., 2003, *A&A*, 397, 675
- Uchida Y., Shibata K., 1985, *PASJ*, 37, 515
- Ustyugova G. V., Koldoba A. V., Romanova M. M., Chechetkin V. M., Lovelace R. V. E., 1995, *ApJ*, 439, L39
- Vernazza J. E., Avrett E. H., Loeser R., 1973, *ApJ*, 184, 605
- Vink J. S., Drew J. E., Harries T. J., Oudmaijer R. D., Unruh Y., 2005, *MNRAS*, 359, 1049
- Walker C., Wood K., Lada C. J., Robitaille T., Bjorkman J. E., Whitney B., 2004, *MNRAS*, 351, 607
- Whitney B. A., Wood K., Bjorkman J. E., Wolff M. J., 2003, *ApJ*, 591, 1049
- Wolf S., Henning T., Stecklum B., 1999, *A&A*, 349, 839
- Wood K., Wolff M. J., Bjorkman J. E., Whitney B., 2002, *ApJ*, 564, 887